Convection for Prandtl numbers near 1: Dynamics of textured patterns

Yuchou Hu,[1,2] Robert Ecke,[1] and Guenter Ahlers[1,2]
[1]*Center for Nonlinear Studies and Materials Division, Los Alamos National Laboratory, Los Alamos, New Mexico 87545*
[2]*Department of Physics and Center for Nonlinear Sciences, University of California, Santa Barbara, California 93106*
(Received 19 September 1994)

Rayleigh-Bénard convection in a cylindrical geometry with radius-to-height ratio $\Gamma=40$ was studied with the shadowgraph imaging method. The working fluid was CO_2 at 32 bars and at temperatures near 34 °C, with a Prandtl number $\sigma=0.98$. The onset pattern of largely straight, parallel rolls went through successive qualitative changes as $\epsilon\equiv\Delta T/\Delta T_c-1$ was increased. Quantitative measurements of wave numbers, of spatially averaged roll curvature, and of sidewall roll orientation as functions of ϵ are presented. As ϵ was increased, pattern dynamics induced by the skewed-varicose instability were first observed at $\epsilon\approx 0.09$, and roll-nucleating sidewall foci were seen for $\epsilon\gtrsim 0.15$. Spiral defects appeared intermittently at $\epsilon\approx 0.55$. The number of spirals fluctuated with time, but the average number increased with ϵ until, at $\epsilon\approx 0.8$, spirals were present at all times. Coincident with the increase in spiral-defect activity was a decrease in the average wave number, a marked increase in the sidewall-foci roll-nucleation frequency and average roll curvature, and a distinct shape change in the structure factor $S(k)$. The oscillatory instability was observed at $\epsilon\approx 3.0$, in agreement with the stability analysis for straight rolls.

PACS number(s): 47.20.−k, 47.27.−i, 47.32.−y

I. INTRODUCTION

Rayleigh-Bénard convection is a model system for pattern formation [1] and has been extensively studied both experimentally and theoretically. Much of the early theory by Busse and Clever [2–4] on the stability of infinitely extended straight, parallel rolls explained many aspects of experimental observations in finite containers, especially those at large Prandtl number $\sigma\equiv\nu/\kappa$ (ν is the kinematic viscosity and κ is the thermal diffusivity). However, textured patterns with roll curvature and nonuniform wave number, observed in the experiments, were not completely described by this approach. This led to the theoretical development of phase-equation descriptions of complex pattern dynamics in Rayleigh-Bénard convection [5–10] and to the recognition that for low-Prandtl-number fluids mean-drift flows are crucial [6,7] to an understanding of the observed complex pattern dynamics [11–15]. Despite impressive theoretical progress, a solid quantitative understanding of such experiments has not been achieved, owing to the difficulty in experimentally measuring mean-drift flows [16] and to the mathematical complexity of the coupled phase and mean-drift equations [9]. Another important factor in most experiments was the limitation in lateral size, measured by the radius-to-height ratio Γ, which was typically less than about 20. Recent experimental results on fluids with σ close to one in large-Γ convection cells with $40<\Gamma<100$ have revealed new phenomena including spiral-defect chaos [17–19] and roll-nucleating sidewall-focus patterns [20,21]. Whereas earlier observations could be tied closely with predicted straight-roll instabilities such as the Eckhaus or skewed-varicose instabilities, these phenomena require explicit consideration of roll curvature and, thus, are natural "objects" for further theoretical study.

Experiments on Rayleigh-Bénard convection in cells of various shapes have demonstrated many of the predictions of straight, parallel-roll instabilities. Busse and Whitehead [22] established semiquantitatively the correspondence between the predicted instabilities of straight rolls [2–4] and experiments by using thermal printing to impose a straight-roll pattern of a desired wave number as an initial condition. The lateral size of their system was so large that their experiments were completed in times much less than a horizontal thermal diffusion time; thus, the lateral boundaries played no role during their observations of the instabilities. Later work by several groups [23–26] investigated steady-state patterns in smaller convection cells, $2<\Gamma<20$, and again found reasonable agreement with theoretical predictions, although some finite-size shifts of stability boundaries were observed. In intermediate-size ($5<\Gamma<12$) cylindrical containers and moderate σ between 2 and 6, the interplay between lateral boundaries and bulk tendencies caused complex textured patterns consisting of curved rolls, defects, and wave-number distortions. These patterns evolved slowly with a multiplicity of possible final steady states arising from austensibly identical initial states [12,13]. In one case [12,14], the evolution to a final state could be described roughly by a Lyapunov functional derived from a Swift-Hohenberg model [27]. This was done by constructing the wave-vector field from the experimental data. This analysis also revealed that under some conditions the wave number k could exceed locally the stability boundaries for straight rolls, providing a qualitative explanation for the unexpected time dependence observed in patterns at small ϵ [12,13]. Variations of the wave number large enough to cause k to be locally outside the theoretical stability limits were also observed in a small-σ experiment [11], where the patterns were time independent for small ϵ but became time dependent

for $\epsilon \approx 0.1$, far below the theoretically expected instability value of about 0.7. In the low-σ experiments, mean-drift flows were believed to be responsible for the observed wave-number distortions. Comparisons for convection cells with and without rigid sidewalls demonstrated the correlation between mean drift, wave-number distortion, and the onset of time dependence [28].

One of the distinct features of many of the experimentally observed patterns in cylindrical convection cells was highly curved rolls in the form of sidewall foci. The origin of these defect structures is in the boundary condition at the lateral wall that favors rolls perpendicular to the sidewall. This tendency increases with ϵ [14,27] so that for $\epsilon > 0.3$ the patterns are dominated by these sidewall foci with more or less complicated defect structures in the interior. The prevalence of foci in patterns suggested that they are important in determining pattern dynamics, and considerable theoretical effort has been directed towards calculating their properties [9]. Concentrating now on experiments for $\sigma \approx 1$, the main results can be understood as a combination of local wave-number instability and nonlocal mean drift. These results for convection cells with $\Gamma \leq 20$ are summarized by Croquette [15]. They have much in common with our present results for $\Gamma = 40$, which we use here to illustrate the phenomena. For $\epsilon < 0.1$, straight, parallel rolls dominated [20], bracketed by small regions of cross rolls, as in Fig. 1(a). For somewhat higher ϵ, wall foci appeared and rolls were squeezed near the center [21]. This led to a skewed-varicose (SV) instability in the interior, as shown in Figs. 1(b) and 1(c). Successive nucleation of rolls at the sidewall foci and absorption of rolls through the SV mechanism produced time dependence, which was periodic or aperiodic depending on conditions. Recent investigations by Bodenschatz *et al.* [17], Morris *et al.* [18,29] (hereafter referred to as MBCA), and by Assenheimer and Steinberg [19,30] revealed complicated curved-roll states including single and multiarmed spirals, targets, and the complex dynamics of spiral-defect chaos (SDC). For our aspect ratio, we found that SDC appeared for $\epsilon \gtrsim 0.55$.

The theory of the dynamics of textured patterns in thermal convection includes many of the ingredients for dynamics in a general pattern-forming system. From one perspective one can consider the stabilities and perturbations about an ordered state, here the straight parallel-roll state. Next a nonuniform distribution of wave numbers is incorporated through a phase equation, a reasonable description when the amplitude is slaved to the wave vector. Finally, the possible interactions of wave-number gradients with the rolls themselves are considered; for convection of fluids with low σ, these interactions arise from mean-drift flows. These theoretical ideas are reviewed extensively by Cross and Hohenberg [1] and alluded to above in descriptions of the experimental investigations. Despite the progress in the inclusion of mean drift, quantitative predictions are still scarce owing to the mathematical complexities of the equations brought about by the nonlocal coupling mediated by the mean-drift field. Even so, very recently work on highly curved rolls has begun, aided by extensive computer modeling. This includes simulations of the Swift-Hohenberg equation with coupled mean drift [31,32] as well as numerical integrations of the Navier-Stokes equations in the Boussinesq approximation [33]. Several of these simulations have demonstrated the robustness of spiral-defect chaos [32,33] and shown some indications of the importance of large aspect ratios for observing these phenomena.

We report here on a systematic investigation of pattern dynamics and wave-number selection for Rayleigh-Bénard convection in a fluid with $\sigma \approx 1$ and for a range $0.05 \leq \epsilon \leq 5$. This paper may be regarded as a sequel to Ref. [20], which dealt with the range $\epsilon \lesssim 0.1$ for similar aspect ratios and σ. We observed the skewed-varicose instability, wall-foci roll nucleation, dislocation-defect dynamics, and the appearance and dynamics of spiral defects. We quantitatively characterized the properties of the patterns using the structure-factor $S(k)$ (the square of the modulus of the spatial Fourier transform) and algorithms that measure the spatial roll curvature and the orientation of the rolls at the lateral sidewalls. The roll-nucleation frequency of wall foci is presented as a function of ϵ. We detected a transition to spiral-defect chaos as indicated by rapid increases in global measures of spa-

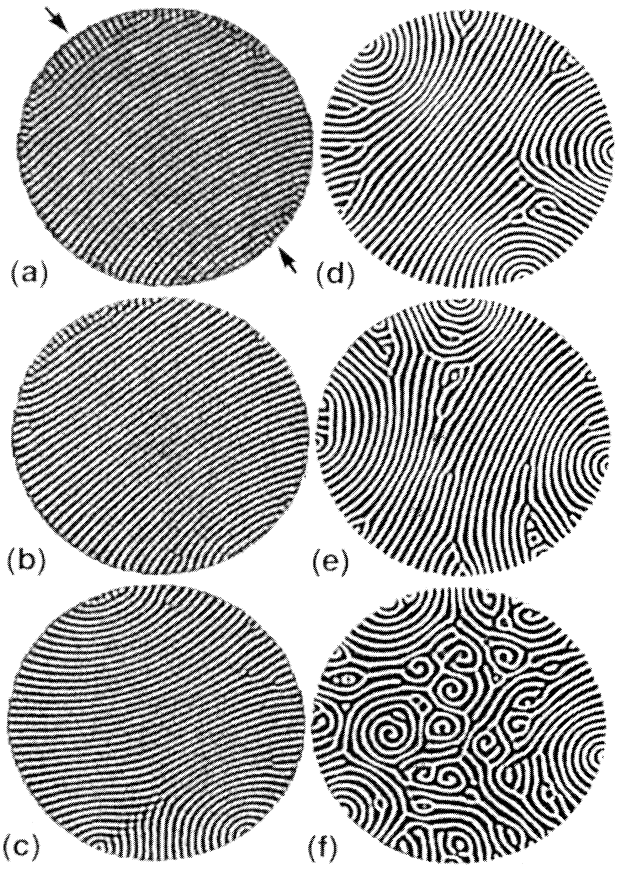

FIG. 1. Representative patterns at $\epsilon =$ (a) 0.04, (b) 0.09, (c) 0.12, (d) 0.51, (e) 0.61, and (f) 0.84. Arrows in (a) point to the cross-roll patches. $\Gamma = 40$.

tial disorder and roll curvature. Our results are compared, when possible, to work in even larger aspect-ratio cylindrical cells that used the same working fluid [17,18,34]. In the remainder of this paper, we present in Sec. II a description of the experiment. Section III gives a qualitative description of the observed pattern dynamics as ϵ was increased. Section IV contains the characterizations of the patterns utilizing structure-factor analysis and algorithms that extract local roll orientation and curvature. Finally, in Sec. V, we discuss our observations and measurements in the context of further work and theoretical modeling. A brief report on some of our work has been presented previously [21,35].

II. EXPERIMENTAL SETUP

The apparatus is described in more detail elsewhere [18,20,36]. The circular paper sidewall used in this study had a cross section shaped like the letter H. The two vertical pieces were both 0.1 mm thick, and one had a diameter of 86 mm and a height of 1.05 ± 0.02 mm while the other had a diameter of 100 mm and a height of 1.03 ± 0.02 mm. The horizontal piece connecting the two vertical pieces was 2.3 mm wide. The actual convection layer studied was enclosed by the 86-mm-diameter ring. This H-shaped design minimized the sidewall thickness seen by the fluid. It reduced the effect of sidewall forcing owing to the fact that the thermal conductivity of paper was ten times larger than that of the fluid [20]. The horizontal piece of the H inhibited convection in the region between the two circular rings and, thus, prevented convection outside the studied region from affecting flow in the interior. The sidewall was sandwiched from the top by a sapphire window and the bottom by an aluminum plate. The sapphire window was held rigidly at its edge, and its vertical position could be adjusted independently of the sidewall at three points separated by about 120°. The uniformity of the cell height d was adjusted to within 0.002 mm by changing the sapphire position. The drawback of this arrangement was the uncertainty in d, as we had no means to measure it directly after all adjustments were finished. We inferred it indirectly through a comparison of ΔT_c with that of a calibration cell with a known cell height operated at the same temperature and pressure [37] and through the assumption that at onset the wave number of the straight-roll structure was the critical wave number, $k_c=3.117$. These two methods gave the same $d=1.06$ mm with an uncertainty of 1%, and an aspect ratio Γ, defined as the ratio of the cell radius to its height, of 40. An additional consideration is that there were places where presumably the sidewall did not make good contact with either the cell bottom or the sapphire plate. These places generated small sidewall foci near the onset of convection, but these foci disappeared for $\epsilon\geq0.05$. The cell was filled with CO_2 at 32 bars and the temperature of the bath that cooled the top plate was held constant within ±0.0002 °C over periods of a week or longer near 33.7 °C. Under these conditions, the fluid has a Prandtl number of 0.98. The pressure was regulated by a temperature-controlled external ballast volume to within 0.005%. The variations of ΔT_c owing to pressure variations were less than 0.01%. Local instabilities such as skewed-varicose defect nucleation occurred on the fast time scale of the vertical thermal diffusion time $\tau_v=d^2/\kappa$, which was 4.8 sec. The time scale of large-scale pattern dynamics was much slower, on the order of or longer than the horizontal thermal diffusion time $\tau_h=\Gamma^2\tau_v$, which was 7680 sec.

The observation of the convection patterns was through the shadowgraph visualization method, and the shadowgraph images were digitized and stored as eight-bit gray-scale-coded images. In this paper, the contrast-enhanced images show black regions corresponding to hot fluid (upflow) and white regions corresponding to cold fluid (downflow). The processing includes first dividing an image with convection by a background image taken in the conduction state, and then rescaling to enhance the contrast [24]. The image division eliminates, to a large extent, the distortions of nonuniformities in illumination and in cell-bottom reflectivity. Various methods of analysis applied to the divided images will be discussed as appropriate in the remainder of this paper. When time-averaged values of parameters were desired, we typically used 256 images at a particular ϵ value. Throughout the work discussed in the present paper, approximately 16 000 images were analyzed.

The determination of ΔT_c was done by quasistatically ramping up ΔT and measuring both the Nusselt number and Fourier power of the convection pattern. The Nusselt number is defined as the ratio of the effective thermal conductivity of the fluid to the thermal conductivity in the conduction state, and the Fourier power is obtained from the structure factor, which is discussed in Sec. IV. Above onset for an ideal system, both Nusselt number and Fourier power vary linearly with ΔT. In our system, there was a slight rounding, and a straight-line fit away from the rounded region yielded $\Delta T_c=1.487\pm0.004$ °C including a small correction, about 1.5%, for the temperature drop across the sapphire window. The rounding was caused by static sidewall forcing, which was not completely eliminated despite the design of the sidewall. Convection appeared in the form of 3–5 circular rings next to the sidewall before the rest of the cell convected. These rings persisted to $\epsilon\approx0.02$, but the rounded region noticeable in the Nusselt number was limited to $-0.005\leq\epsilon\leq0.007$ with the value of the Nusselt number less than 1.003 at $\epsilon=0$. The Prandtl number, equal to 0.98, was calculated with the virial equation of state at the mean temperature, 34.45 °C, of the fluid layer at the onset of convection. The kinematic viscosity was 0.002 32 cm^2/sec, and the thermal diffusivity was 0.002 38 cm^2/sec. The non-Boussinesq parameter P [38] was 0.22, considerably smaller than the P values of MBCA.

III. PATTERN DYNAMICS

A consequence of the large lateral dimension of the system is that, near onset, pattern evolution is very slow, taking 3–10 days to reach a final steady state when ΔT is increased slowly from below onset. To speed up this process, we increased ϵ to ≈1 where the pattern was highly

time dependent, and then reduced ϵ to approximately 0.04. This method usually yielded a straight-roll pattern like that in Fig. 1(a) within 36 h. The two small sidewall foci on the upper right region were presumably caused by gas flowing in or out of the cell, and they disappeared at $\epsilon=0.05$. Such patterns were time independent for $\epsilon<0.09$. Over this range, the size of the cross-roll patches, indicated by arrows in Fig. 1(a) and bracketing the main straight-roll region, typically decreased somewhat with increasing ϵ [20].

The first instability of the straight-roll pattern was the skewed-varicose instability at $\epsilon\approx0.09$. The scenario was as reported earlier [15,20], with defects nucleating *via* the pinching off of rolls in the central region of the cell and then moving to the sidewall. Details of this mechanism are illustrated in Fig. 2. These images were taken in the $\Gamma=41$ cell of Ref. [20], but the observations in our present cell are very similar. Some defects disappeared upon reaching the wall, whereas others remained or moved along the wall to disappear into the cross-roll patches. A typical image at $\epsilon=0.09$ is shown in Fig. 1(b). The two defects on the lower right part of the cell eventually disappeared into the cross rolls at the lower right. The left defect moved to merge with the upper left cross rolls. This locally occurring skewed-varicose instability has been shown to be the result of a large-scale flow coupled to roll curvature and wave-number gradients [28]. A useful way to show the defect nucleations *via* the skewed-varicose instability is to plot the angular distribution of the modulus of the Fourier transform as a function of time. Figure 3(a), at $\epsilon=0.12$, is such a plot constructed from 43 images covering a time interval of $6\tau_h$. It is coded in a linear gray scale with the maximum black and the minimum white. When there is a dominant roll orientation, the power is concentrated around that orientation; but, when roll pinching occurs, the power is more dispersed owing to the defects. The numerous skewed-varicose defect-nucleation events appear as the discontinuities in the width of the narrow dark vertical band, which indicates the dominant roll orientation as a function of time. Whereas the nucleation of defects happened on the local time scale τ_v, the interval between nucleations was of the order of the global time scale, about $0.4\tau_h$ for the data shown in Fig. 3(a).

Further increases of ϵ caused faster defect nucleations and more defect accumulations near the wall. The straight rolls near the cross rolls also began to curve measurably as the tendency for the rolls to end perpendicularly to the sidewall increased with ϵ. At $\epsilon\approx0.12$, sidewall foci occasionally appeared as the result of defects merging with the cross rolls. The foci would often contain cross rolls unless the instantaneous curvature around the foci was large. These foci interacted with defects and were constantly annihilated and regenerated, but the new focus typically appeared a few roll widths away and contained cross rolls. In Fig. 1(c), we show a focus containing cross rolls at the upper left and a well-defined focus at the lower right. To the left of the well-defined focus is a line of defects (grain boundary) where differently oriented rolls join. In this particular example, these defects merged with the focus, resulting in a new focus with cross rolls.

At $\epsilon\approx0.20$, the roll curvature was large enough that foci were always present. There were typically two foci with radii of about $20d$. As ϵ increased, the number of foci also increased but their individual sizes decreased. At $\epsilon\approx0.50$, there were typically 4–7 foci each measuring

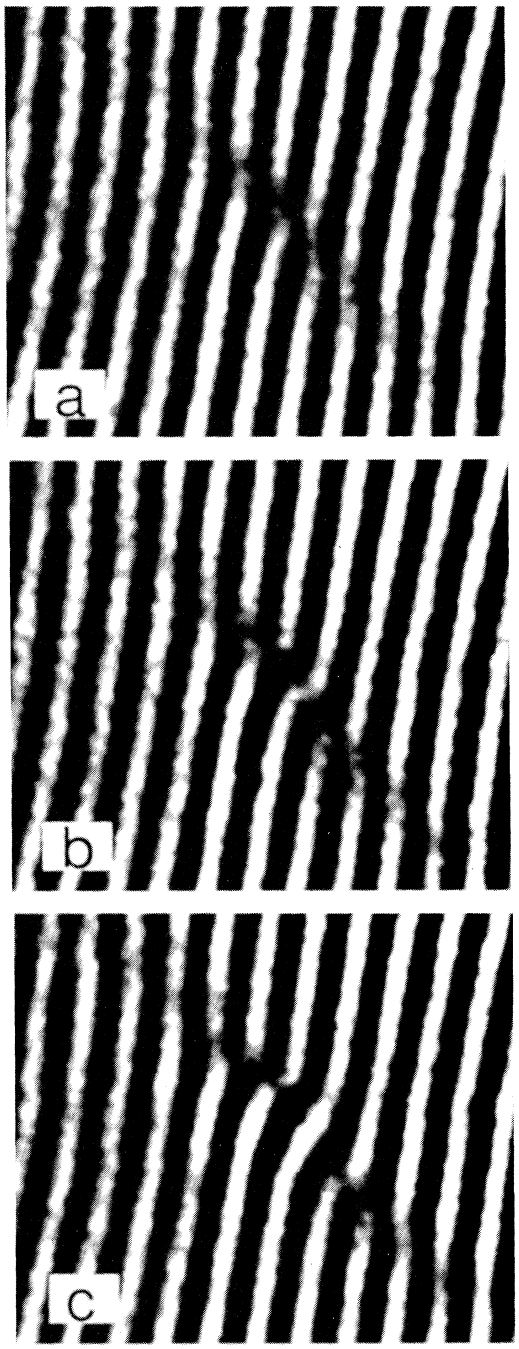

FIG. 2. Defect nucleation mechanism for straight rolls at $\epsilon=0.115$ and for $\Gamma=41$. A fraction of the total image, about $22d$ on a side, is shown. Elapsed times (arb. orig.) are (a) 0.0, (b) 1.3, and (c) $2.6\tau_v$.

about $(6-8)d$ in radius. For $\epsilon \geq 0.20$, these foci generally nucleated new rolls [21,39] while moving irregularly along the sidewall. The frequency of the roll nucleation ω_n, expressed in units of $1/\tau_v$, varied a little for a given focus but increased substantially when the focus was near a defect or another focus. For well-isolated foci ω_n varied linearly with ϵ up to $\epsilon \approx 0.65$ as shown in Fig. 4. A linear-least-squares fit to the data gave $\omega_n = 0.17(\epsilon - 0.16)$. Around a well-isolated focus, the time dependence could be attributed to skewed-varicose-instability events and focus roll nucleation. At the interface between a focus and the still indentifiably straight-roll region, skewed-varicose instability formed defects and at the same time reduced the local wave number (a roll pinching-off created two defects but reduced the number of roll pairs by one). At the center of the focus, the nucleation of a new roll would increase locally the wave number around the focus. So the interplay between the skewed-varicose instability at the focus periphery and the nucleation of new rolls at the focus center gave rise to sustained time dependence locally around the well-isolated focus. It is important to remember that, owing to the large-scale flow coupling these local pattern features over a long range, the global dynamics cannot be described solely in term of these local events. For example, this simple picture is altered as soon as a defect comes near the center of the focus or when two foci approach each other.

A further demonstration of the nonlocal interaction is found in the comparison of two possible states for $0.2 < \epsilon < 0.3$, where both 2-foci and 3-foci states were observed depending on past history. The time dependence of the foci was dramatically different for the two states despite the similarities of the foci, illustrating that the global configuration of the rolls was important in the pattern dynamics. An example of the 3-foci state is shown in Fig. 5(a). The growth of an additional focus from a grain boundary between the original two foci [the ones on the right side in Fig. 5(a)] changed the characteristics of the original ones. Instead of nucleating new rolls, they absorbed rolls, but at a frequency a factor of 3–4 smaller than that of nucleating foci at the same ϵ. Defect formation via the skewed-varicose instability near the focus periphery slowed down or stopped completely. The dominant time dependence then occurred in the vicinity of the remaining grain boundary, which is shown in the enclosed rectangular box in Fig. 5(b). In this region, rolls switched their orientation rapidly, alternating between two directions as shown in Fig. 5(c), which is a blowup of the enclosed region in Fig. 5(b). Rolls of one orientation grew into regions occupied by rolls of the other orientation, but these rolls at the same time were being replaced

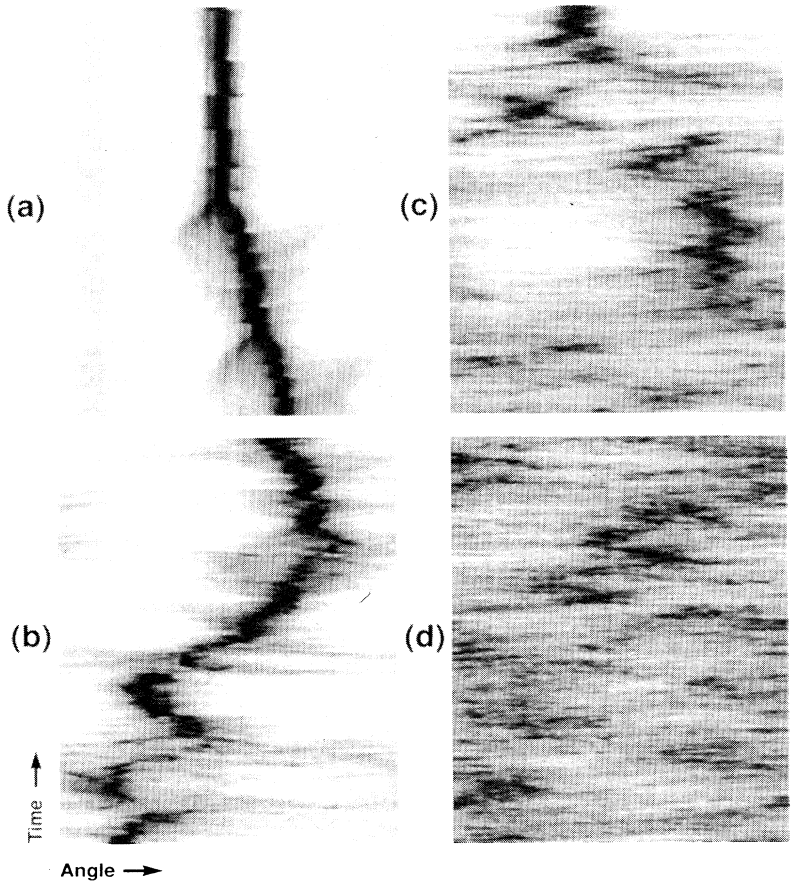

FIG. 3. Gray-scale plot (black:high) of the angular distribution $(0 < \theta < \pi)$ of the modulus of the Fourier transform as a function of time. The ϵ values and the total time covered are (a) $\epsilon = 0.12$, $6.0\tau_h$; (b) $\epsilon = 0.61$, $11.4\tau_h$; (c) $\epsilon = 0.69$, $11.4\tau_h$; and (d) $\epsilon = 0.78$, $11.4\tau_h$.

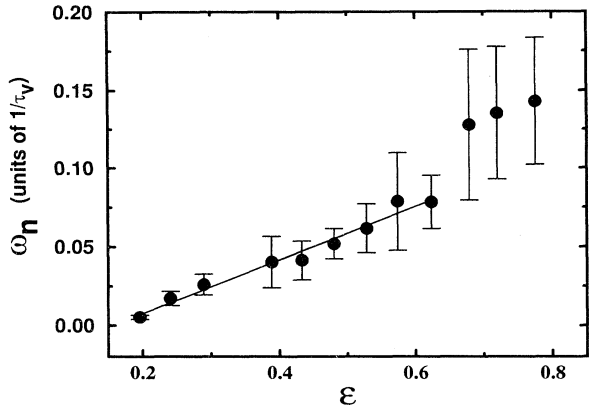

FIG. 4. Foci roll-nucleation frequency ω_n as a function of ϵ. The vertical bars indicate the standard deviation of the distribution of frequencies. The solid line is a linear fit to the data for $\epsilon < 0.63$.

by rolls of the other orientation at the trailing edge. The net effect was a set of differently oriented domain boundaries that traveled from a point near the center of the focus along this line of defects. This same dynamics generated new rolls even as the original two foci absorbed rolls, so the number of rolls in the system remained fairly constant. Such a 3-foci pattern was remarkably stable compared to a 2-foci pattern. In a 2-foci pattern, the foci were generally destroyed and regenerated with an average period of $2\tau_h$, whereas in a 3-foci pattern the three foci remained for between 6 to $12\tau_h$. The 3-foci state invariably gave way to the 2-foci state when ϵ was decreased to below 0.2, but the long evolution time prevented the determination of the asymptotic pattern at a fixed ϵ between 0.2 and 0.3.

The roll-nucleation frequency increased with ϵ while the average size of foci decreased as seen in Figs. 1(c)–1(e). An abrupt increase in ω_n of about 40% occurred at $\epsilon \approx 0.65$ as seen in Fig. 4. This change was associated with the appearance of the SDC state [18,21] as shown in Fig. 1(f). This state contained many rotating and merging spirals, which could have one or two arms and could be right- or left handed. The amount of time for one rotation of a spiral was variable but typically was of the order of $10\tau_v$. In the early stage, a spiral often appeared as a concentric-ring pattern, but this "target" would merge with the roll next to it to form a spiral. A time series of images showing some scenarios for spiral formations is presented in Fig. 6. These are similar to the formation mechanisms described by Assenheimer and Steinberg [19]. The arrows in Fig. 6 highlight the formation of two separate spirals; the one on the left originated from a line segment while the one on the right started as a "broken" spiral. The transition into the spiral-defect state was continuous and occurred over a narrow range in ϵ. At $\epsilon \approx 0.53$, pointlike defects appeared sporadically from regions resembling grain boundaries. These pointlike defects were short lived and generally stayed within a distance of $10d$ from the wall. At $\epsilon \approx 0.6$, these defects appeared more often and also grew in size, sometimes forming circular structures measuring only $(3-4)d$ across; some of these structures evolved into recognizable spiral structures and actually traversed the width of the whole cell. Figure 1(e) contains such a circular structure at the lower right and a small point defect near the top. The formation of spirals was intermittent in the sense that there was an ϵ range just above 0.6 over which spirals were present only some of the time. This intermittency is seen best again in a plot of the angular distribution of the radially averaged Fourier-transform magnitude because

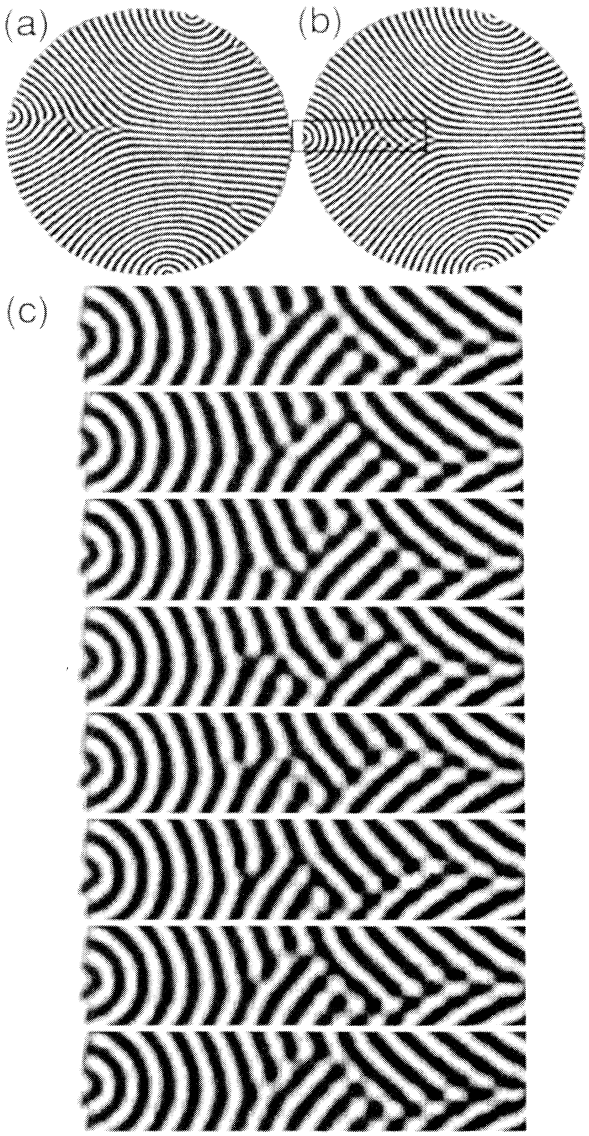

FIG. 5. Representative 3-foci patterns. (a) and (b) are separated in time by $6000\tau_v$. (c) A time sequence, $48\tau_v$ apart, of the region outlined in (b). The top image in (c) corresponds to the image enclosed by the box in (b).

spirals contribute power to all angles. In Fig. 3(b), $\epsilon=0.61$, we see that the spirals only existed during the time interval when the power was dispersed. At $\epsilon=0.69$, Fig. 3(c), about half of the time there were lots of spirals. At $\epsilon=0.75$, spirals were formed and destroyed continuously as shown by the widely dispersed power in Fig. 3(d).

Once the spirals appeared, further increases in ϵ brought no real changes in the pattern dynamics until the appearance of the oscillatory instability at $\epsilon\approx 3$, in good agreement with the predictions of stability analysis for straight rolls [2]. The oscillatory instability manifested itself as waves traveling along the rolls as indicated by the arrows in Fig. 7, which shows only a portion of the cell. The oscillation period was about $1\tau_v$. Even at $\epsilon\approx 4$ where these images were recorded, the traveling waves existed only locally, and they did not appear throughout most of the cell until $\epsilon\approx 5.5$. The traveling waves on rolls ending at the sidewall always propagated toward the wall; so, for a roll with both ends connected to the wall, there was always a source of traveling waves near its midpoint. Associated with the fast dynamics of the traveling waves was the comparatively slow rearrangement of the underlying roll patterns. This is evident in a comparison between Figs. 7(a) and 7(b), which are $78\tau_v$ apart.

IV. CHARACTERIZATION OF PATTERNS

Characterization of complex time-dependent patterns remains a major challenge in the experimental investigation of pattern dynamics. The patterns ideally should be described by a small set of parameters, which capture their essential aspects. Unfortunately, to our knowledge, no theoretical works exist that point to such a set of parameters. We have employed standard techniques to characterize the patterns by their wave numbers, wave number distributions, average roll curvature, and average roll orientation adjacent to the sidewall. These parame-

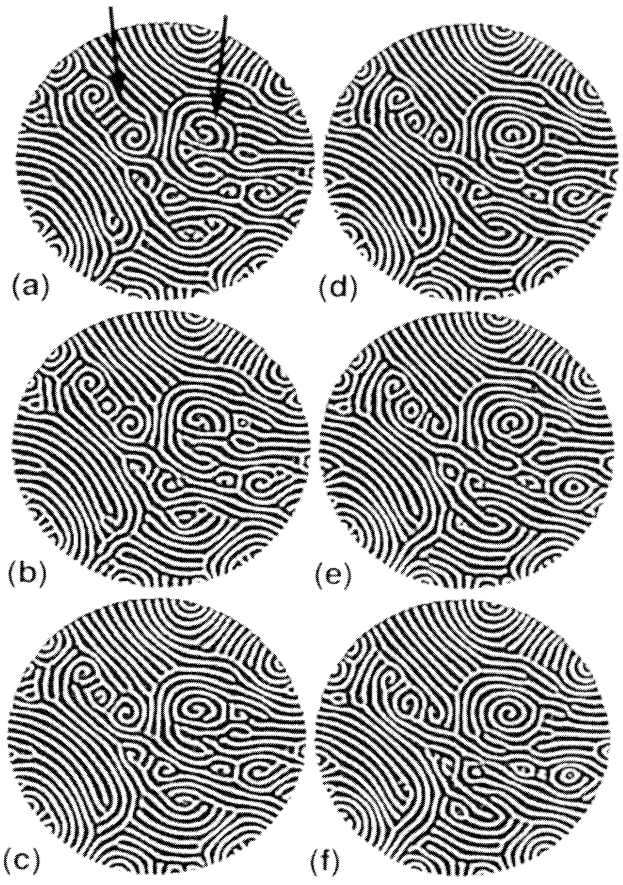

FIG. 6. Formation of spirals at $\epsilon=0.70$. The images are $6.4\tau_v$ apart. The arrows point to two structures that evolved into spirals.

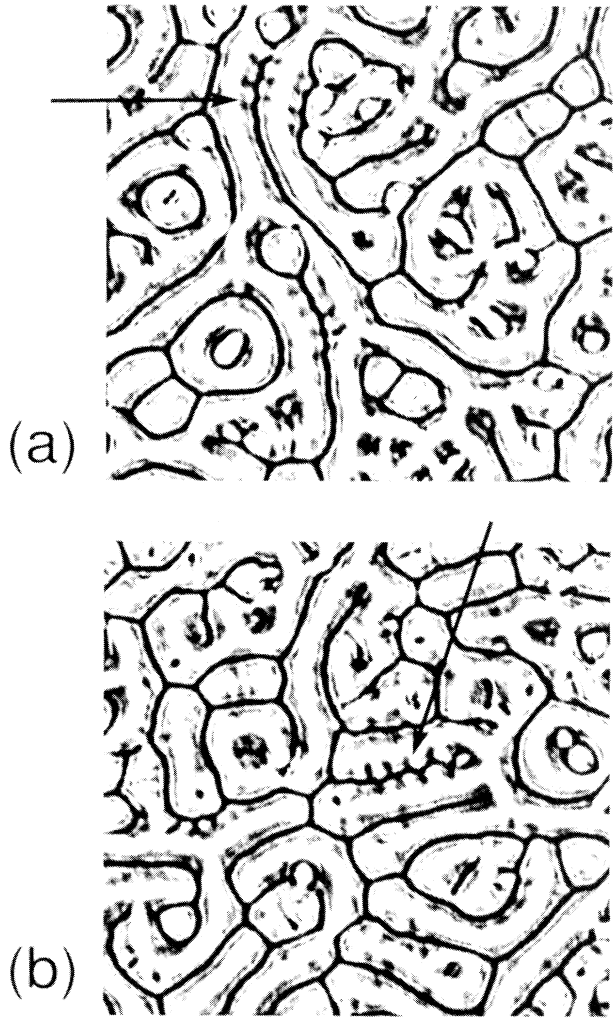

FIG. 7. Oscillatory instability at $\epsilon\approx 4.0$. The images are $78\tau_v$ apart. The arrows indicate the traveling waves.

ters do not give a complete description, but their interpretation provides a first step in our understanding of the patterns and their dynamics.

A. Structure factor

The structure factor, equal to the modulus squared of the spatial Fourier transform, provides information that is averaged over the whole pattern since spatial information is lost as the phase of the Fourier transform is discarded. The calculations of various quantities from the structure factor follow closely the procedures used by Morris *et al.* [18,40]. The structure factor $S_i(\vec{k})$ of the ith image in a sequence of images taken at the same ϵ was obtained by the following steps. The image was first divided into the background, because this division preserved the linearity of the mapping of the vertically averaged temperature field of the fluid layer to the shadowgraph signal [20,41] over a wider range of ϵ. The divided image was filtered by a radial Hanning window $H(r)\equiv[1+\cos(\pi r/r_0)]/2$ for $r\leq r_0$ and $H(r)\equiv 0$ for $r>r_0$, $r_0=0.71\Gamma$. A discrete Fourier transform on the filtered image was performed to get the modulus squared, $S_i(\vec{k})$. An average over all $S_i(\vec{k})$ taken at the same ϵ gave $S(\vec{k})$. From this time-averaged $S(\vec{k})$, statistics such as the average wave number $\langle k\rangle$, the correlation length ξ defined to be the inverse of the width s_2, and the skewness s_3 were calculated [18]. The definitions for these quantities are

$$\langle k\rangle\equiv\frac{\int|\vec{k}|S(\vec{k})d^2\vec{k}}{\int S(\vec{k})d^2\vec{k}}=\frac{\int_0^\infty k^2S(k)dk}{\int_0^\infty kS(k)dk}\ , \tag{1}$$

$$\xi^{-1}\equiv s_2\equiv\left[\frac{\int(|\vec{k}|-\langle k\rangle)^2S(\vec{k})d^2\vec{k}}{\int S(\vec{k})d^2\vec{k}}\right]^{1/2}$$

$$=\left[\frac{\int_0^\infty(k-\langle k\rangle)^2kS(k)dk}{\int_0^\infty kS(k)dk}\right]^{1/2}\ , \tag{2}$$

$$s_3\equiv\left[\frac{\int(|\vec{k}|-\langle k\rangle)^3S(\vec{k})d^2\vec{k}}{s_2^3\int S(\vec{k})d^2\vec{k}}\right]^{1/3}$$

$$=\left[\frac{\int_0^\infty(k-\langle k\rangle)^3kS(k)dk}{s_2^3\int_0^\infty kS(k)dk}\right]^{1/3}\ . \tag{3}$$

In practice, the calculation did not extend from $k=0$ to $k=\infty$ but only included values of k for which $kS(k)$ was greater than 15% of the maximum value of $kS(k)$. The limit of 15% was chosen to be a suitable limit applicable up to $\epsilon=5$. At $\epsilon\approx 1$, the shadowgraph nonlinearity manifested itself as higher harmonics in $kS(k)$, but a 15% limit excluded the higher harmonics quite well up to $\epsilon\approx 3.5$. In Fig. 8, we show examples of $kS(k)$ averaged over many patterns and over angle for several ϵ values. In Fig. 9, we show an average over k to yield $S(\theta)$, the angular power distribution. Figure 3 is composed of many curves corresponding to $\sqrt{S(\theta)}$ and offset in time.

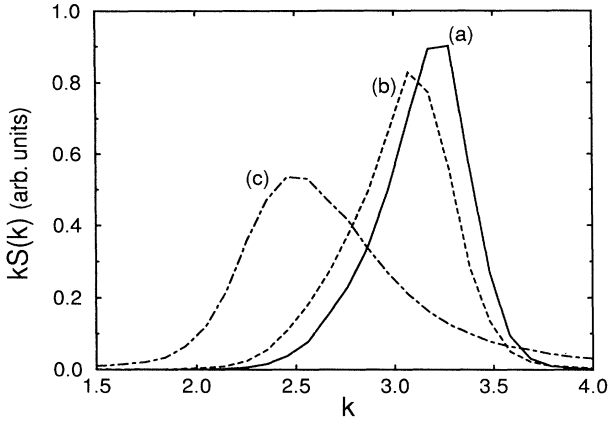

FIG. 8. $kS(k)$ for (a) $\epsilon=0.46$, (b) $\epsilon=0.61$, and (c) $\epsilon=0.81$.

The application of the structure factor derived from the Fourier transform to many areas of physics is well established [42]. Its use for the analysis of textured patterns in relatively small systems, however, is not as well understood. In particular, the effects of defects, wave-number distribution, pattern type, and finite size can be complicated. Application of the structure-factor algorithm to artificial patterns [43] suggests a cautious approach in interpreting the results. The main conclusion of the study was that the sidelobe contributions in the Fourier-transform peak shape cannot be neglected and that different pattern types with otherwise uniform and identical wave number have quite different peak shapes, yielding significantly different values for $\langle k\rangle$ and also for higher moments. For example, in a system with about 350 rolls, $\langle k\rangle$ can vary by 4% and s_2 by almost 200% between straight and concentric rolls. The variation also depends on the limits in k over which the moments are calculated. One should conclude that for systems of finite

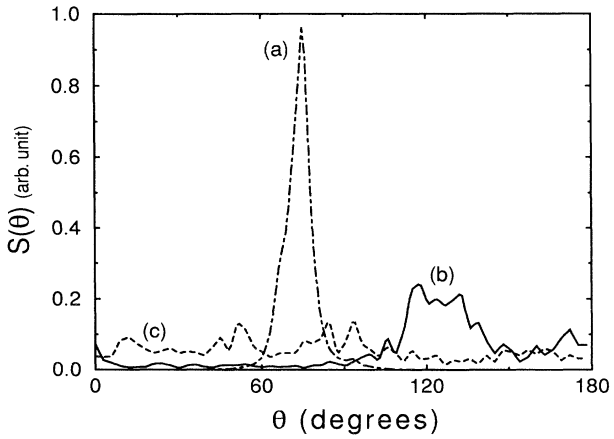

FIG. 9. $S(\theta)$ for (a) $\epsilon=0.46$, (b) $\epsilon=0.61$, and (c) $\epsilon=0.81$.

size caution is necessary especially since the influences of defects and wave-number distribution have not been systematically studied. With this caveat, we proceed to analyze the experimental images using the $S(k)$ procedure; it has the attractive feature of being well defined and easy to use on many images.

While the selected wave number for straight-roll patterns has been studied theoretically and experimentally, it is not clear for a textured pattern full of defects and curved rolls what the selected average wave number should be. A recent theoretical analysis by Newell, Passot, and Souli [44] suggested that in textured patterns containing many curved rolls the wave number selected would be close to that of a concentric-roll pattern at least for time-independent patterns [45–47]. We shall see that this does not seem to be the case for our system and that the problem with wave-number selection in textured patterns remains unresolved. We define the selected wave number to be the average wave number $\langle k \rangle$, and normalized $\langle k \rangle$ to be 3.117 (k_c) at $\epsilon=0$ to compensate for the uncertainty in d.

Near onset, the system had a straight-roll pattern within the circular region covered by the applied Hanning window. The selected wave number increased with ϵ as seen in Fig. 10 which plots our observations in terms of $\langle k \rangle - k_c$. The increase was accompanied by changes in the sizes of the cross-roll patches bracketing the straight rolls. The grain boundary between the cross rolls and the straight rolls in the interior presumably provided the wave-number-selection mechanism for the straight rolls [20]. Also plotted in Fig. 10 are the selected wave numbers for similar straight-roll patterns in a $\Gamma=43$ cell, for which the wave number was calculated by locally fitting a sine function to the rolls while assuming that $\langle k \rangle$ was 3.117 at $\epsilon=0$ [20]. The data agree quite well, showing that the wave numbers calculated from the structure factor describe the straight rolls as well as local

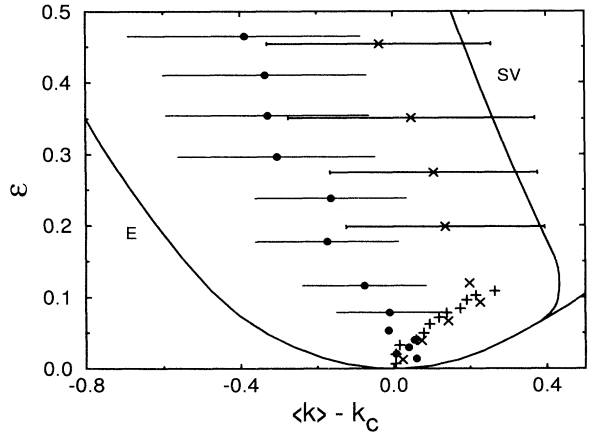

FIG. 10. Phase diagram near onset. (×) current cell with $\Gamma=40$, $\sigma=0.98$; (+) $\Gamma=43$, $\sigma=0.93$; (●) $\Gamma=78$, $\sigma=0.95$ from MBCA. *E*, Eckhaus; and SV, skewed-varicose instability boundaries (adapted from Refs. [2] and [3]). The horizontal bars on some of the data have a length equal to s_2.

fits which cannot be performed easily on patterns with defects and curved rolls.

It is interesting to contrast the grain-boundary selection mechanism with a similar one investigated for large-Prandtl-number $\sigma=70$ in a rectangular geometry [48]. In that case, grain-boundary wave-number selection was shown to coincide with that of dislocation selection; both were in close agreement with the condition that the perpendicular diffusion constant in the phase equation $D_\perp$ equals zero. This condition in turn corresponds to the boundary at low wave number for the zig-zag instability. This description works very nicely for large Prandtl number, but in low-Prandtl-number convection, mean drift stabilizes against the zig-zag instability and no previous experiments or theory have addressed the selection of wave number by dislocations or grain boundaries in that case. Our results, Fig. 10, show that some different mechanism was responsible since the condition $D_\perp=0$ operates at low wave number, whereas our average wave number increased unexpectedly with ϵ up to the onset of time dependence. It would be useful in exploring this selection to consider a rectangular cell similar to that used in [48] to minimize the possible effects of sidewall curvature in a cylindrical geometry. It would also help to measure, if possible, the velocity and selected wave number for isolated defects in this low Prandtl system to better quantify this new wave-number-selection mechanism.

At $\epsilon\approx0.09$, $\langle k \rangle$ began to decrease with increasing ϵ. This was accompanied by the appearance of defect formation via the skewed-varicose instability in the system interior. Further ϵ increases brought about sidewall foci and increased roll curvature; $\langle k \rangle$ maintained roughly the same distance from the skewed-varicose instability boundary up to $\epsilon\simeq0.55$. In Fig. 10 we also show, for comparison, data from a $\Gamma=78$ circular cell at $\sigma=0.95$ from MBCA [49]. In that experiment, the measured cell height was used to set the length scale, whereas we normalized $\langle k \rangle$ at $\epsilon=0$ to k_c. A detailed comparison for $\epsilon<0.5$ is difficult because MBCA did not concentrate on this regime. In particular, they did not have a high enough density of ϵ values to determine unambiguously the behavior of $\langle k \rangle$ for $\epsilon<0.05$ or for $\epsilon\approx0.25$. These two regions are of interest as discussed below. Nevertheless, some general features of the two data sets can be compared. The MBCA data did not approach the SV instability boundary and may or may not have the increase in $\langle k \rangle$ observed in this work; the data are consistent with either a small increase for $\epsilon<0.05$ or a monotonic decrease with ϵ. The source of this difference is unclear since the qualitative appearance of the patterns (except for the system size) was similar to ours for ϵ up to about 0.25, i.e., they were dominated by straight rolls for $\epsilon\lesssim0.1$ and by curved rolls and sidewall foci for larger ϵ. For $\epsilon\simeq0.25$, MBCA observed the onset of SDC. Their results for $\langle k \rangle$ showed only a small (if any) change in their ϵ dependence near this value. This differs from our smaller cell, in which the onset of SDC did not begin until $\epsilon\approx0.55$. As shown in Fig. 11, beyond that ϵ value $\langle k \rangle$ decreased more rapidly and moved further away from the SV instability boundary. For $\epsilon\gtrsim0.75$, well into

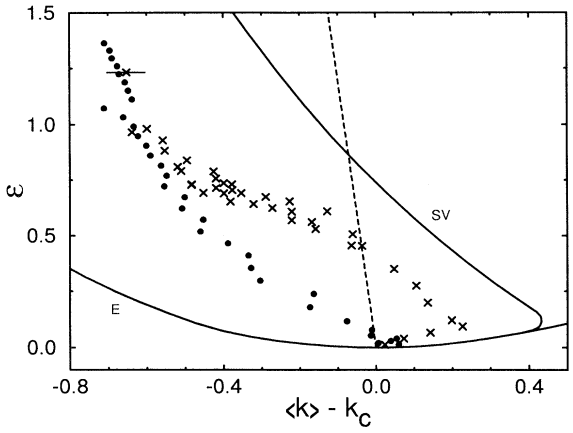

FIG. 11. Phase diagram over a larger ϵ range. (×) current cell with $\Gamma=40$, $\sigma=0.98$; (●) $\Gamma=78$, $\sigma=0.95$ from MBCA. *E*, Eckhaus; and SV, skewed-varicose instability boundaries (adapted from Refs. [2] and [3]). Dashed line, predicted $\langle k \rangle - k_c$ for concentric patterns [47].

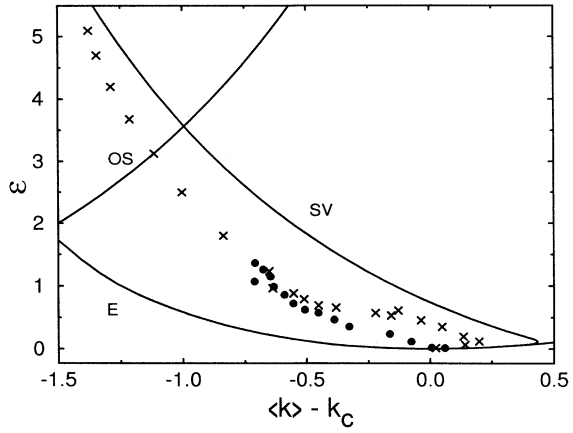

FIG. 12. Phase diagram over a very large range of ϵ. (×) current cell with $\Gamma=40$, $\sigma=0.98$; (●) $\Gamma=78$, $\sigma=0.95$ from MBCA. *E*, Eckhaus; SV, skewed varicose; and OS, oscillatory instability boundaries (adapted from Refs. [2] and [3]).

the spiral-defect state for both cells, the average wave numbers for the two systems were the same within experimental uncertainty.

The predicted wave number for concentric patterns [46] crosses the skewed-varicose boundary near $\epsilon=0.8$ as shown in Fig. 11. It does not agree with measured wave numbers in the experiments. Thus, the conjecture by Newell, Passot, and Souli [44] that the concentric-pattern wave-number-selection mechanism might set the average wave number in textured patterns owing to the presence of sidewall foci does not seem to apply for time-dependent states in either the $\Gamma=40$ or 78 convection system with $\sigma\approx 1$. This idea seemed to work reasonably well [44] in describing experimental observations for somewhat higher Prandtl number [14], $\sigma=2.5$, and in a moderate-aspect-ratio container, $\Gamma\approx 14$. The origin of this inconsistency is unclear. It may be the result of the larger aspect ratios in the CO_2 experiments, which perhaps permit a different mechanism unrelated to sidewall foci to dominate the wave-number selection in the system interior.

At higher ϵ, the basic spiral formation and destruction remained qualitatively the same, but the overall wave number decreased as seen from Fig. 12. The average wave number never crossed the skewed-varicose boundary and instead crossed the oscillatory instability boundary at $\epsilon\approx 3$. At ϵ slightly less than 3, the oscillatory instability was visible locally. Presumably this is due to the existence of a wave-number distribution, with the local k below the oscillatory instability in some places.

In addition to $\langle k \rangle$, higher moments of the structure factor may also be used to convey information about the patterns. The correlation length ξ, defined in Eq. (2) to be the inverse of the standard deviation of $S(k)$, represents roughly the average size of correlated regions in the system. In Fig. 13, we show how ξ varied with ϵ in our experiment. The correlation length decreased monotonically with increasing ϵ and varied as $(2.8\pm0.3)\epsilon^{-0.42\pm0.09}$, very close to the variation of $(2.4\pm0.1)\epsilon^{-0.43\pm0.05}$ reported in MBCA. One should note that, in MBCA, spiral defects appeared at $\epsilon\approx 0.25$; therefore, most of the data from that study were from patterns with spirals. In our system, spiral defects did not appear until the much higher ϵ of 0.6, so the closeness of the two exponents and the coefficients may be indicative of the insensitivity of ξ to the details of the specific underlying pattern.

The third moment of the structure factor, the skewness s_3, provides a measure of the relative contributions of wave numbers higher or lower than the average, i.e., of the distribution asymmetry. We found that it was a useful indicator of the transition to the spiral-defect-chaos state. The decrease of s_3 right above onset, Fig. 14, was caused by the formation of defects via the skewed-varicose instability. Once the skewed-varicose instability appeared, s_3 remained fairly constant until spirals ap-

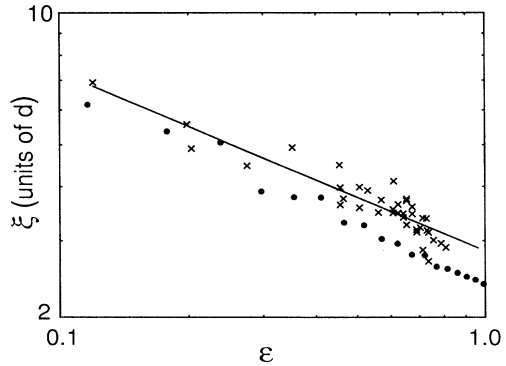

FIG. 13. Correlation length ξ vs ϵ. (×) current cell with $\Gamma=40$ and $\sigma=0.98$; (●) $\Gamma=78$ and $\sigma=0.95$ from MBCA. The solid line is a least-squares fit to the data with $\xi=2.8\epsilon^{-0.42}$.

peared at $\epsilon \approx 0.6$. It then increased rapidly with ϵ until spirals were always present for $\epsilon \gtrsim 0.8$. The increase in s_3 is consistent with a slightly larger effective wave-number contribution from concentric pattern types such as targets or spirals [43].

What is not clear from $s_3(\epsilon)$ is the fluctuating nature of spiral formation. This is revealed in plots such as those of Fig. 3, which give time series of the radially averaged modulus of the Fourier transform, i.e., of the radial average of the square root of $S_i(\vec{k})$. Individual examples of $S(\theta)$ are shown in Fig. 9. To quantify the intermittency, we defined the intermittency fraction F_I as the fraction of time for which the standard deviation of the angular power distribution was greater than 30° [50]. The cutoff of 30° was somewhat arbitrary, but the results were not very sensitive to this choice. The fraction grew from 0 for no spirals to 1 for continuous spiral formation: It corresponded very well with changes in the skewness (see Fig. 14). Detailed analysis of the statistics of individual spiral defects presented elsewhere [51] yields conclusions similar to those derived from the global measures presented here.

B. Roll curvature and sidewall obliqueness

Phase dynamics descriptions of textured patterns include significant contributions from roll curvature and from the sidewall boundary condition that favors rolls perpendicular to the boundary. Thus, a quantitative measure of these influences would provide an important characterization of textured patterns in low-Prandtl-number convection. Previously Heutmaker and Gollub [14] were able to obtain some information on the spatially averaged curvature $\langle |\vec{\nabla}\cdot\vec{n}| \rangle$ and sidewall obliqueness $\langle |\vec{n}\cdot\vec{s}| \rangle$, where $\vec{n}$ is the unit wave vector and $\vec{s}$ is the sidewall normal vector. In a $\Gamma = 10$ circular cell, they showed that up to $\epsilon \approx 3$ and for averages over a number of patterns, the curvature increased and obliqueness decreased with increasing ϵ. With the manually interactive procedure that they employed, only a small number of ϵ values could be considered and only a modest number of patterns could be averaged. We extended this analysis to many patterns and to a large number of ϵ values by developing an automatic procedure for obtaining roll orientation and roll curvature.

Our algorithm for determining local roll orientation and curvature includes several steps, which are indicated in Fig. 15. First, the gray-scale image of a convection

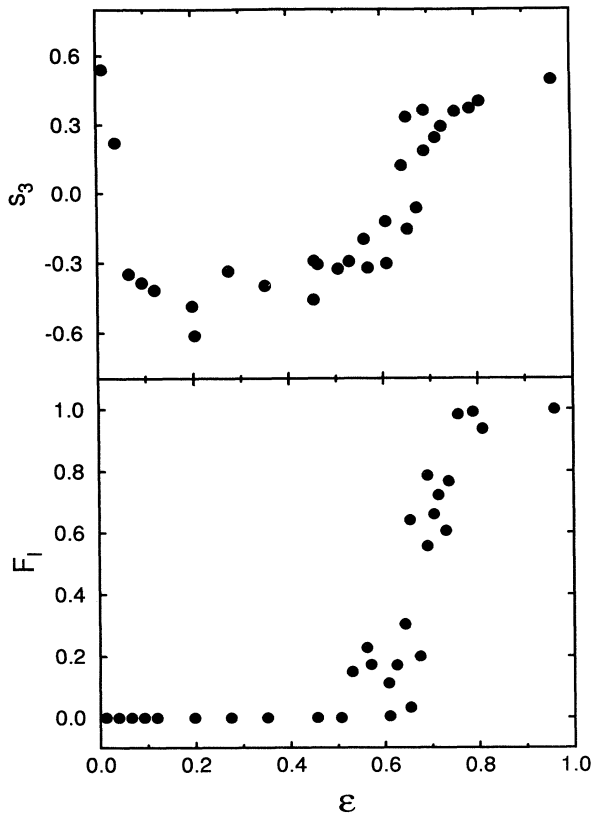

FIG. 14. Skewness s_3 and intermittent fraction F_I vs ϵ.

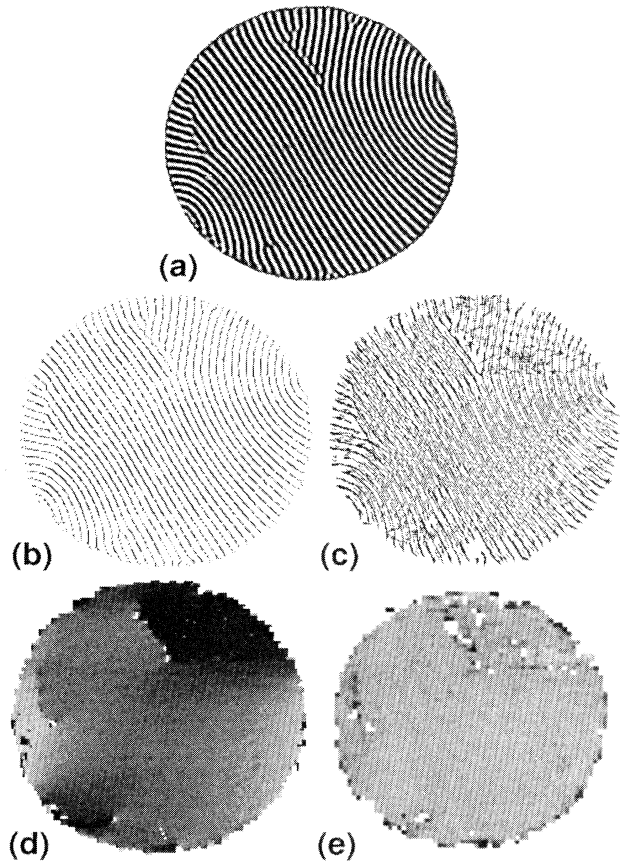

FIG. 15. Illustration of the procedure for determining roll orientation and curvature. The image is for $\epsilon = 0.11$. (a) Original thresholded image, (b) skeleton-line image, (c) reconstruction of image based on calculated local orientation, (d) orientations (darker equals small angle with zero angle corresponding to the horizontal axis), and (e) curvatures (darker equals large curvature).

pattern is thresholded so that only black or white pixel values remain [Fig. 15(a)]. Then a standard algorithm [52] is used to produce a skeleton-line representation of the original pattern [Fig. 15(b)]. Next, a rectangular mesh with grid points at every other pixel is superimposed on top of the line image. At every grid point, a local line segment consisting of typically 5–10 pixels (one wavelength is approximately equal to six pixels) is extracted. The extraction is based on a 10×10 pixel window. A least-squares fit of a straight line to these data is then performed to obtain the local orientation. The calculated orientations for Fig. 15(a) are shown in gray scale in Fig. 15(d), where black regions represent small angles, and the angles are measured between the roll axis and the horizontal axis, increasing in the counterclockwise direction. If the residual of the fit exceeds some preset limit, then the obtained value is discarded; typically this occurs at regions of highly curved rolls, at defects, or at crossings of rolls. These regions are shown in white. Local roll curvatures γ are obtained in similar fashion with a fit to a parabola as shown in Fig. 15(e), where black regions represent large curvatures but the white regions are where the procedures do not yield valid values. The window size for the roll curvature is variable, changing from 14×14 pixel down to 8×8 pixel; the change is adapted to the detailed local roll structures. The algorithm works quite well, as seen in Fig. 15(c), which is a reconstructed image based on the calculated local roll orientations. Whereas the example image in Fig. 15 contains mostly slightly curved rolls, the algorithm works equally well for spirals, as shown by Fig. 16. In Fig. 16(d), we note that spirals yield a clockwise arrangement of alternating black

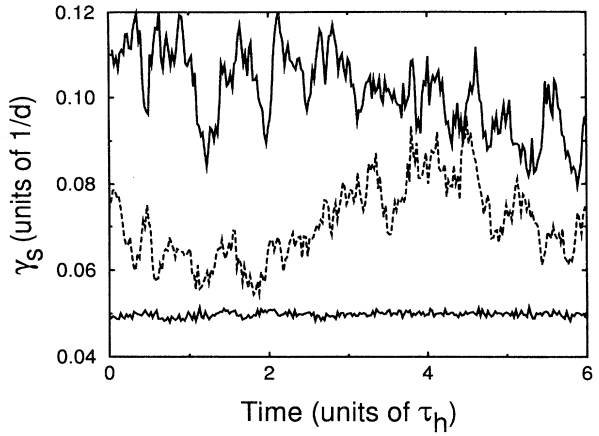

FIG. 17. Spatially averaged curvature γ_s vs time. Lower solid line, $\epsilon=0.35$; dashed line, $\epsilon=0.65$; and upper solid line, $\epsilon=0.81$.

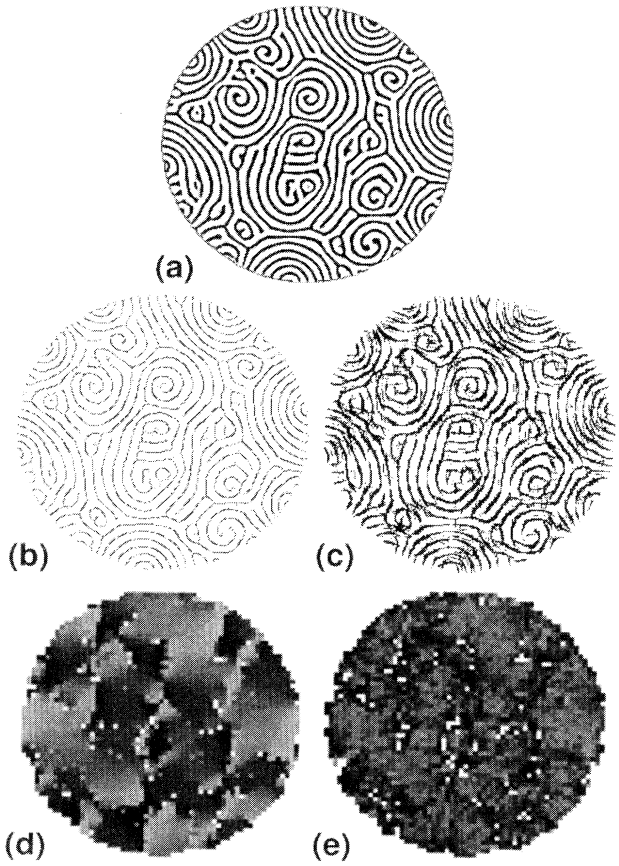

FIG. 16. Illustration of the procedure for determining roll orientation and curvature. The image is for $\epsilon=0.88$. (a) Original thresholded image, (b) skeleton-line image, (c) reconstruction of image based on calculated local roll orientations, (d) roll orientations (darker equals small angle with zero angle corresponding to the horizontal axis), and (e) curvatures (darker equals large curvature).

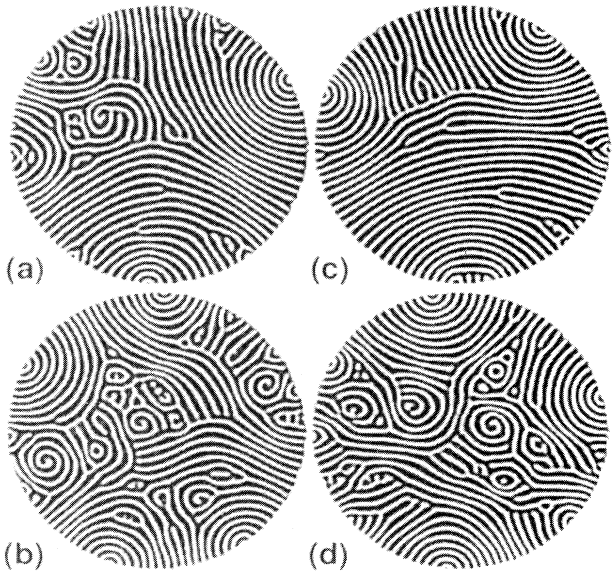

FIG. 18. Representative images at $\epsilon=0.73$. (a)–(d) correspond to the points indicated in Fig. 22.

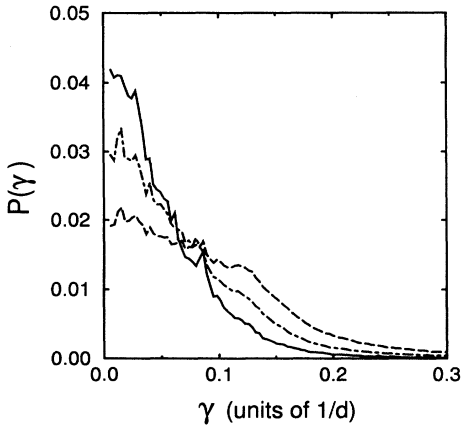

FIG. 19. Probability distribution $P(\gamma)$ of the curvatures γ. Solid line, $\epsilon=0.35$; dash-dotted line, $\epsilon=0.65$; and dashed line, $\epsilon=0.81$.

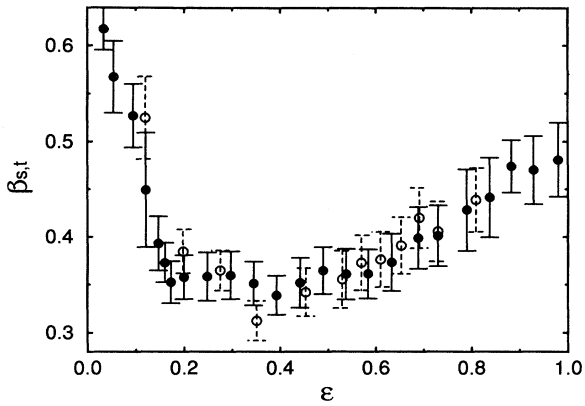

FIG. 21. Spatially and temporally averaged sidewall obliqueness $\beta_{s,t}$ vs ϵ. The vertical bars indicate the standard deviation of the distribution of β at a particular ϵ. The solid circles are for decreasing, and the open circles for increasing ϵ.

and white quadrants with the first quadrant being white. The interfacial regions between two spirals are similarly represented, except the first quadrant is black. The curvature of a roll measures the angle traversed per unit arc length along the roll and is the inverse of the radius of curvature [53], so for a spiral the curvature gets larger with decreasing distance from the center of the spiral.

Because of increased video noise near the cell edges, the average roll-curvature calculation was limited to a circular region for $r \leq 38d$, where r is measured from the center of the cell. For the sidewall obliqueness calculations, the increased noise affects the precise determination of roll orientations next to the sidewall; unfortunately, this effect could not be avoided since, by definition, the obliqueness is calculated next to the wall.

The spatially averaged curvature γ_s as a function of time is shown for several values of ϵ in Fig. 17. Below the onset of SDC, at $\epsilon=0.35$, γ_s did not change appreciably with time since the patterns were composed mostly of large sidewall foci. At $\epsilon=0.81$, where SDC was well developed, spirals were present at all times but their number and sizes fluctuated considerably as indicated by the variation in γ_s. In the transition region, $0.55 \leq \epsilon \leq 0.8$, γ_s changed significantly, from less than 0.06 corresponding to almost no spirals to 0.12 corresponding to many spirals. These large changes in γ_s reflect the possible patterns the system could have at the same ϵ. For example, at $\epsilon=0.73$, there could be no spirals as shown in Fig. 18(c), which looks very similar to Fig. 1(d) at $\epsilon=0.51$, or there could be many spirals as in Fig. 18(d), which is similar to Fig. 1(f) at $\epsilon=0.84$.

Figure 19 plots the probability distribution of the local curvature γ for the same ϵ values as in Fig. 17. As expected, the fraction of highly curved rolls increased with increasing ϵ while the fraction of straighter rolls decreased. The time and spatially averaged curvature $\gamma_{s,t}$

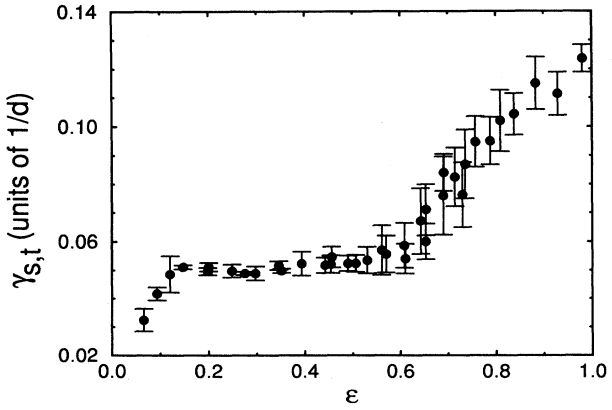

FIG. 20. The spatially and temporally averaged curvature $\gamma_{s,t}$ vs ϵ. The vertical bars indicate the standard deviation of the distribution of γ at a particular ϵ.

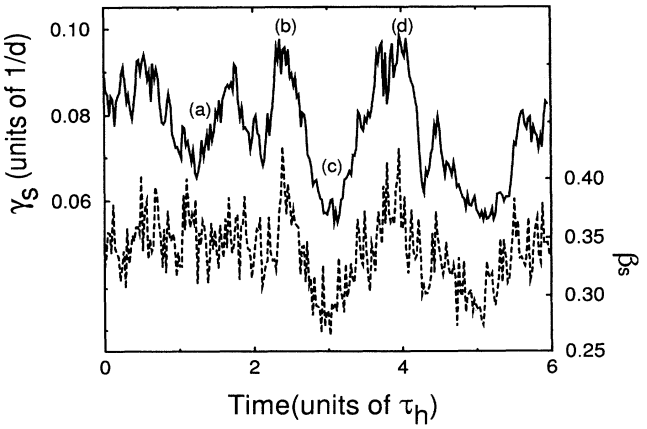

FIG. 22. Spatially averaged curvature (solid line) and spatially averaged sidewall obliqueness (dashed line) at $\epsilon=0.73$ as functions of time. The points (a)–(d) correspond to the images in Fig. 18.

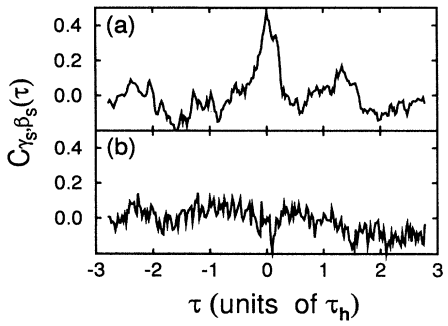

FIG. 23. Cross correlations $C_{\gamma_s,\beta_s}(\tau)$ between the spatially averaged curvature and the spatially averaged sidewall obliqueness. (a) $\epsilon=0.69$ and (b) $\epsilon=0.28$.

as a function of ϵ is shown in Fig. 20. The increase near $\epsilon=0.1$ is readily identified with the appearance of defects owing to the skewed-varicose instability and of sidewall foci, whereas the increase near $\epsilon=0.6$ corresponds to the appearance of spirals. An interesting result is that $\gamma_{s,t}$ hardly varied over the wide range of $0.2\lesssim\epsilon\lesssim0.55$. This contradicts the general notion that roll curvature should increase continuously with ϵ as suggested by phase-dynamics descriptions of pattern dynamics in finite systems [1].

The sidewall obliqueness measures the extent to which rolls terminate at the sidewall with their axes perpendicular to the wall. The boundary condition at the wall favors rolls ending more nearly perpendicular to the wall as ϵ is increased [1]. This tendency has been demonstrated to be responsible for the formation of sidewall foci and for the associated depressed onset of the skewed-varicose instability [15]. We measured the obliqueness, $\beta=|\vec{n}\cdot\vec{s}|$, via the dot product of the sidewall normal vector and the normalized wave vector of the rolls adjacent to the wall, so if the roll joined the wall perpendicularly, the value would be 0. In Fig. 21, two separate runs are presented for the time and spatially averaged obliqueness $\beta_{s,t}$. The data taken while ϵ was decreased did not differ significantly from those taken during a run with ϵ increasing. We note that the data for decreasing ϵ were much shorter in duration (about ten times) than for the increasing data set. The ϵ dependence was very similar for the two cases with the rolls becoming more and more perpendicular (smaller β) to the wall with increasing ϵ for $\epsilon\lesssim0.3$. For $0.3\lesssim\epsilon\lesssim0.6$, the obliqueness was relatively constant but with the appearance of spiral-defect chaos, rolls ended less and less perpendicular (larger β) to the wall as ϵ increased above 0.6. Both the constant value of β at moderate ϵ and the increase at higher ϵ were unexpected based on previous measurements [12,14].

The average curvature is a global measure over a large area of the cell, while the obliqueness is restricted to a narrow band next to the sidewall. This raises the question of whether these two quantities are related, and if so, whether they are correlated in time. In Fig. 22 are plots of γ_s and β_s for $\epsilon=0.73$, and representative images are shown in Fig. 18. The cross-correlation calculations between $\gamma_s(t)$ and $\beta_s(t)$ show that the obliqueness was strongly correlated with the average curvature, and that the correlation was instantaneous to within our experimental time resolution of $50\tau_v$. The cross-correlation coefficients $C_{\gamma_s,\beta_s}(\tau)$, where τ denotes the lag time, between γ_s and β_s are shown in Fig. 23 for two values of ϵ. It is interesting to note that at $\epsilon=0.28$, γ_s and β_s were uncorrelated; but, as SDC appeared in the system, γ_s and β_s were positively correlated. Note that the fact that the *average* values of $\gamma_s(t)$ and $\beta_s(t)$ were roughly constant for ϵ below 0.5, the temporal *fluctuations* about the mean were not correlated. The correlation coefficients at zero time lag for different values of ϵ are plotted in Fig. 24. For $0.2\lesssim\epsilon\lesssim0.5$, γ_s and β_s were not correlated, and for $\epsilon>0.6$, the correlation increased but saturated at about 0.35.

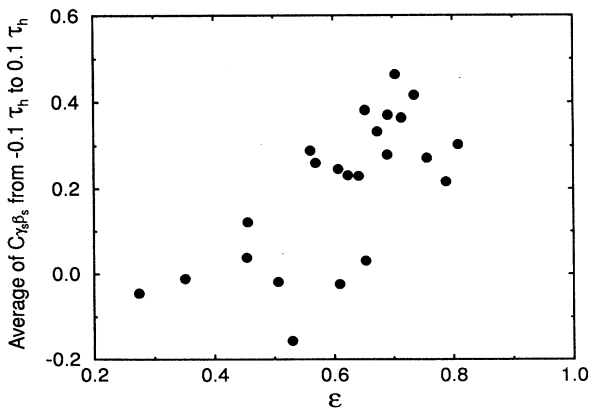

FIG. 24. Cross correlation at zero time lag $C_{\gamma_s,\beta_s}(\tau=0)$ between the spatially averaged curvature and the spatially averaged sidewall obliqueness as a function of ϵ. The average of $C_{\gamma_s,\beta_s}(\tau)$ over the interval $-0.1\tau_h\lesssim\tau\lesssim0.1\tau_h$ is shown.

V. CONCLUSION

In this paper, we have presented experimental observations of pattern dynamics in a large-aspect-ratio system with a Prandtl number near 1. The initial time-dependent straight-roll patterns at onset first became unstable at $\epsilon=0.09$ to the skewed-varicose instability enhanced by global mean drift. The tendency for rolls to end perpendicularly to the sidewall increased with ϵ for $\epsilon<0.2$ and produced large sidewall foci, which often emitted but occasionally absorbed rolls. The typical frequency of the roll emissions by the foci increased linearly with ϵ. Below the onset of spiral defect chaos, the dynamics were dominated by defect nucleation via the skewed-varicose instability and new roll creations by the focus instability. Large-scale global flow was apparent in the interactions among the various defects and foci, but was difficult to analyze quantitatively. The time scale for dynamics in this parameter range was comparable to τ_h for the time between nucleation of defects, although the time scale for the nucleation event itself was more nearly τ_v.

The onset of spiral-defect chaos occurred at $\epsilon=0.55\pm0.04$. The spiral formation was intermittent slightly above its onset. The fraction of time over which spirals existed in the system increased from 0 below onset to nearly 100% at $\epsilon=0.8$. This transition is interesting from the perspective of determining the mechanism for spiral-defect chaos. Perhaps it can shed some light on the degree to which mean drift is important in creating and/or sustaining spiral defects. We hope that some of the characterizations we have used to analyze the state of the system may yield clues to the mechanisms for time dependence and spiral-defect creation. We now review the results reported earlier in this paper with an eye towards these issues.

We first consider the average wave numbers of the patterns, determined through structure-factor analysis. The average wave number increased unexpectedly for $\epsilon<0.09$, owing to a lateral boundary cross-roll selection mechanism [20]. After the onset of time dependence resulting from dislocation-defect nucleation at $\epsilon\approx0.09$, $\langle k \rangle$ decreased monotonically with increasing ϵ, maintaining approximately constant distance from the theoretical skewed-varicose boundary. At $\epsilon\approx0.55$, there was a rapid decrease of about 0.35 in $\langle k \rangle$ over the interval of fluctuating spiral nucleation. The change in slope of $\langle k \rangle$ occurred approximately where $\langle k \rangle$ crossed the theoretical focus selection curve. This is suggestive but perhaps coincidental since there are appreciable differences in the ϵ dependence of $\langle k \rangle$ for cells of different aspect ratios. For example, the $\langle k \rangle$ data of MBCA with $\Gamma=78$ showed little or no increase in $\langle k \rangle$ at small ϵ and were always smaller than the focus wave number. Another observation is that the decrease in $\langle k \rangle$ at the onset of SDC was much smaller for MBCA (we estimate no larger than 0.1) than for our smaller cell with $\Gamma=43$. The significance of these two observations is unclear and further experimental and theoretical work will be needed to understand the selection of the average wave number in this system and the role, if any, which this plays in the formation of spiral-defect chaos.

Structure-factor analysis, in addition to yielding the average wave number, provided a measure of the distribution of wave number through the peak shape. The second and third moments were used to define a spatial correlation length and the peak-shape asymmetry or skewness. The correlation length was not particularly sensitive to pattern changes and varied approximately like $\epsilon^{-1/2}$. The skewness, on the other hand, was quite responsive to pattern variations and provided a good operational means for determining the onset of spiral defect chaos. The change of the shape of $S(\vec{k})$, which produced an easily measurable change in the skewness over the transition interval leading to fully developed spiral-defect chaos, is consistent with a larger contribution from spirals or targets to the peak distribution.

Other important characterizations for the pattern dynamics reported here are the average roll curvature and sidewall obliqueness. These two quantities help measure the relative influence of bulk versus surface (i.e., lateral boundary) contributions to the pattern dynamics. The notion of boundary-induced frustration coupled with roll curvature and mean drift has been quite successful in describing the slow dynamics in the dislocation-defect regime. So it is important to understand the interaction of these quantities as well as their individual dependences on ϵ. The unexpectedly constant value of the curvature between $0.2\lesssim\epsilon\lesssim0.6$ and the increase in both the curvature and sidewall obliqueness after the onset of SDC are interesting trends. So too is the appreciable correlation between curvature and obliqueness in the SDC regime. Thus, the picture of phase-dynamic frustration seems pretty good in the dislocation-defect regime with increasing curvature and decreasing sidewall obliqueness. In the SDC regime, however, this picture apparently breaks down quite dramatically. The time scale for defect motions, both spiral and other, decreases so that it is now much faster, of order ten times τ_v. The rapid increase in the curvature is no surprise since spirals and targets are highly curved objects. The increase in sidewall obliqueness and the moderate degree of correlation between curvature and obliqueness above the SDC onset suggests that sidewall effects are overwhelmed by the spiral state, being driven by the behavior of the bulk rather than imposing structure on it. Another reflection of this may be the increase in nucleation frequency of sidewall foci. After the transition, there are typically more sidewall foci of smaller size. Perhaps the frequency increases with decreasing size. We have not made a systematic investigation of this point. Finally, it is clear that our characterization is incomplete in an important way. A more complete characterization of the phase dynamics would include a local determination of the complete wave-vector field so that the wave-number distribution could be calculated directly since the global measure determined through Fourier transform techniques is not very sensitive nor accurate for single images. We hope to resolve this in future work.

For $\epsilon\gtrsim0.8$, the wave numbers for the spiral-chaos state matched closely those measured in an aspect-ratio 78 system [18]. At even higher ϵ, the oscillatory instability was observed. The onset of the oscillatory instability at $\epsilon\approx3.0$ occurred at an average wave number, which agreed with the stability analysis of infinitely extended straight rolls [2]. The roll oscillations were superimposed on slower time dynamics of the pattern, which was similar to that below the oscillatory onset. The wave motion on the rolls was complex, consisting of both standing and traveling waves with numerous sinks and sources for the traveling waves. One noticeable feature for traveling waves was that waves on rolls that terminated at the lateral boundary always traveled towards the sidewalls.

In summary, many questions remain unanswered about low-Prandtl-number convection in a spatially extended system away from the convective onset. Whereas this study has concentrated on particular features of the dynamics such as the focus instability or the spiral-defect-chaos state, the interactions of different regions of the cell via globally coupling mean flows were not studied directly. The characterizations of individual robust features like the focus emission frequency provided only the first steps in the characterization of the complex spatiotemporal dynamics that we observed. Statistical methods employed in this study such as the structure-factor

analysis or intermittency fraction in angle-time plots are unable to completely elucidate the time evolution of the patterns. One thing is abundantly clear to us in the analysis and interpretation of these experimental data. Very large numbers of images are required to achieve reasonable statistics; thus, automated and highly robust analysis algorithms are necessary for progress to be made. Although we have made a good start, further analysis tools are needed to characterize these complicated patterns and to interpret current and future experimental data.

ACKNOWLEDGMENTS

We gratefully acknowledge support from a UC/LANL INCOR grant and from the U.S. Department of Energy. We thank Ning Li, Stephen Morris, and David S. Cannell for useful discussions on the characteristics of structure factors; Eberhard Bodenschatz, John de Bruyn, David S. Cannell, Stephen Morris, and Steve Trainoff for their contributions to the design of the apparatus; and Mike Cross and Werner Pesch for discussion regarding the behavior of spirals as seen in numerical simulations.

[1] M. C. Cross and P. C. Hohenberg, Rev. Mod. Phys. **65**, 851 (1993).
[2] R. M. Clever and F. H. Busse, J. Fluid Mech. **65**, 625 (1974).
[3] F. H. Busse and R. M. Clever, J. Fluid Mech. **91**, 319 (1979).
[4] F. H. Busse, in *Hydrodynamic Instabilities and the Transition to Turbulence,* edited by H. Swinney and J. P. Gollub (Springer-Verlag, Berlin, 1981), p. 97.
[5] Y. Pomeau and P. Manneville, J. Phys. Lett. **40**, L609 (1979).
[6] E. Siggia and A. Zippelius, Phys. Rev. Lett. **47**, 835 (1981).
[7] M. C. Cross, Phys. Rev. A **27**, 490 (1983).
[8] M. C. Cross and A. C. Newell, Physica D **10**, 299 (1984).
[9] A. C. Newell, T. Passot, and M. Souli, J. Fluid Mech. **220**, 187 (1990).
[10] A. C. Newell, T. Passot, and M. Souli, Eur. J. Mech. B **1**, 151 (1991).
[11] A. Pocheau, V. Croquette, and P. Le Gal, Phys. Rev. Lett. **55**, 1094 (1985).
[12] M. S. Heutmaker, P. N. Fraenkel, and J. P. Gollub, Phys. Rev. Lett. **54**, 1369 (1985).
[13] G. Ahlers, D. S. Cannell, and V. Steinberg, Phys. Rev. Lett. **54**, 1373 (1985).
[14] M. S. Heutmaker and J. P. Gollub, Phys. Rev. A **35**, 242 (1987).
[15] V. Croquette, Contemp. Phys. **30**, 153 (1989).
[16] The experimental difficulties of measuring weak global flows in the presence of dominant local roll circulations are formidable; the only direct characterization of mean flows in convection was a study by Croquette *et al.* for a static pattern [54].
[17] E. Bodenschatz, J. R. de Bruyn, G. Ahlers, and D. S. Cannell, Phys. Rev. Lett. **67**, 3078 (1991).
[18] S. W. Morris, E. Bodenschatz, D. S. Cannell, and G. Ahlers, Phys. Rev. Lett. **71**, 2026 (1993).
[19] M. Assenheimer and V. Steinberg, Nature **367**, 345 (1994).
[20] Y. Hu, R. E. Ecke, and G. Ahlers, Phys. Rev. E **48**, 4399 (1993).
[21] Y. Hu, R. E. Ecke, and G. Ahlers, Phys. Rev. Lett. **72**, 2191 (1994).
[22] F. H. Busse and J. A. Whitehead, J. Fluid Mech. **47**, 305 (1974).
[23] J. P. Gollub, A. R. McCarriar, and J. F. Steinman, J. Fluid Mech. **125**, 259 (1982).
[24] V. Steinberg, G. Ahlers, and D. S. Cannell, Phys. Scr. **32**, 534 (1985).
[25] P. Kolodner, R. W. Walden, A. Passner, and C. M. Surko, J. Fluid Mech. **163**, 195 (1986).
[26] V. Croquette, Contemp. Phys. **30**, 113 (1989).
[27] M. C. Cross, Phys. Rev. A **25**, 1065 (1982).
[28] F. Daviaud and A. Pocheau, Europhys. Lett. **9**, 675 (1989).
[29] S. W. Morris, E. Bodenschatz, D. S. Cannell, and G. Ahlers, Bull. Am. Phys. Soc. **37**, 1734 (1992).
[30] M. Assenheimer and V. Steinberg, Phys. Rev. Lett. **70**, 3888 (1993).
[31] M. Bestehorn, M. Fantz, R. Friedrich, and H. Haken, Phys. Lett. A **174**, 48 (1993).
[32] H.-W. Xi, J. D. Gunton, and J. Vinals, Phys. Rev. Lett. **71**, 2030 (1993).
[33] W. Decker, W. Pesch, and A. Weber, Phys. Rev. Lett. **73**, 648 (1994).
[34] S. W. Morris, E. Bodenschatz, D. S. Cannell, and G. Ahlers (unpublished).
[35] Y. Hu, R. E. Ecke, and G. Ahlers, Phys. Rev. Lett. **74**, 391 (1995).
[36] J. R. de Bruyn, E. Bodenshatz, S. W. Morris, S. Trainoff, Y. Hu, D. S. Cannell, and G. Ahlers (unpublished).
[37] This cell had $d=1.031\pm0.005$ mm and gave $\Delta T_c=1.51\pm0.01$ °C.
[38] F. H. Busse, J. Fluid Mech. **30**, 625 (1967).
[39] We regret that a mistake was made in Fig. 4 of Ref. [21]. The correct unit for the vertical axis was $300/\tau_h$.
[40] $S(k)$ was referred to in MBCA as the *structure function.* Here we use the common nomenclature of *structure factor* from condensed matter physics, as, for example, in [42].
[41] S. Rasenat, G. Hartung, B. I. Winkler, and I. Rehberg, Exp. Fluids **7**, 412 (1989).
[42] D. L. Goodstein, *States of Matter* (Prentice-Hall, Engelwood Cliffs, NJ, 1975).
[43] Y. Hu, L. Ning, and R. E. Ecke (unpublished).
[44] A. C. Newell, T. Passot, and M. Souli, J. Fluid Mech. **220**, 187 (1990).
[45] P. Manneville and J. M. Piquemal, Phys. Rev. A **28**, 1774 (1983).
[46] J. C. Buell and I. Catton, J. Fluid Mech. **171**, 477 (1986).
[47] J. C. Buell and I. Catton, Phys. Fluids **29**, 23 (1986).
[48] A. Pocheau and V. Croquette, J. Phys. (Paris) **45**, 35 (1984).
[49] S. W. Morris, a +3% correction to $\langle k \rangle$ has been applied to the published data of MBCA resulting from an improved measurement of d for that convection cell; (private communication).
[50] The standard deviation for patterns with a dominant roll orientation was typically between 15° and 25°.
[51] R. E. Ecke, Y. Hu, R. Mainieri, and G. Ahlers (unpublished).

[52] The medial axis algorithm was provided by UNM's KHOROS package, which implements morphological algorithms from C. Giardina and E. Dougherty, *Morphological Methods in Image and Signal Processing* (Prentice-Hall, Englewood Cliffs NJ, 1988).

[53] The curvature calculated with this algorithm is $\frac{1}{2}$ that of the alternative definition of $|\vec{\nabla}\cdot\vec{n}|$ [14].

[54] V. Croquette, P. Le Gal, A. Pocheau, and R. Guglielmetti, Europhys. Lett. **1**, 393 (1986).

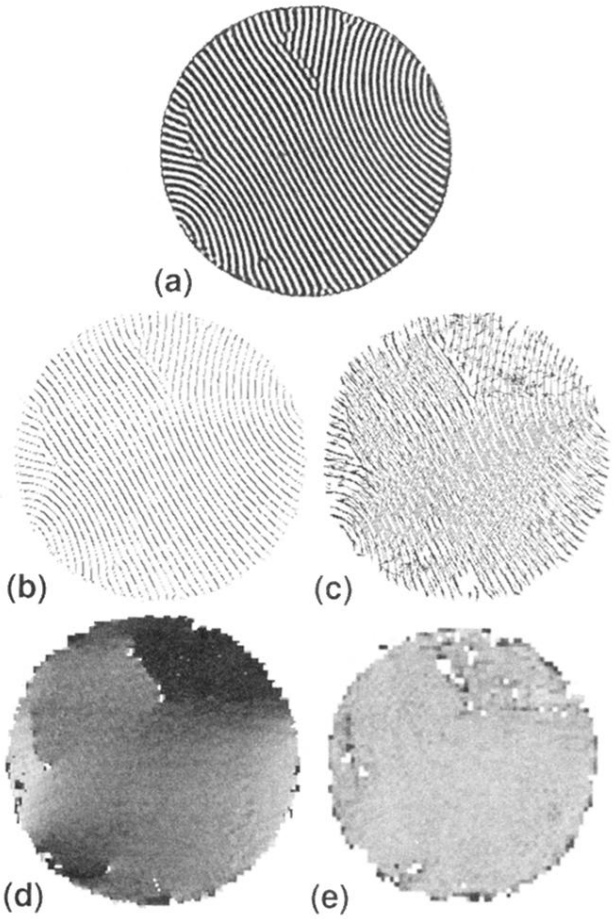

FIG. 15. Illustration of the procedure for determining roll orientation and curvature. The image is for $\epsilon=0.11$. (a) Original thresholded image, (b) skeleton-line image, (c) reconstruction of image based on calculated local orientation, (d) orientations (darker equals small angle with zero angle corresponding to the horizontal axis), and (e) curvatures (darker equals large curvature).

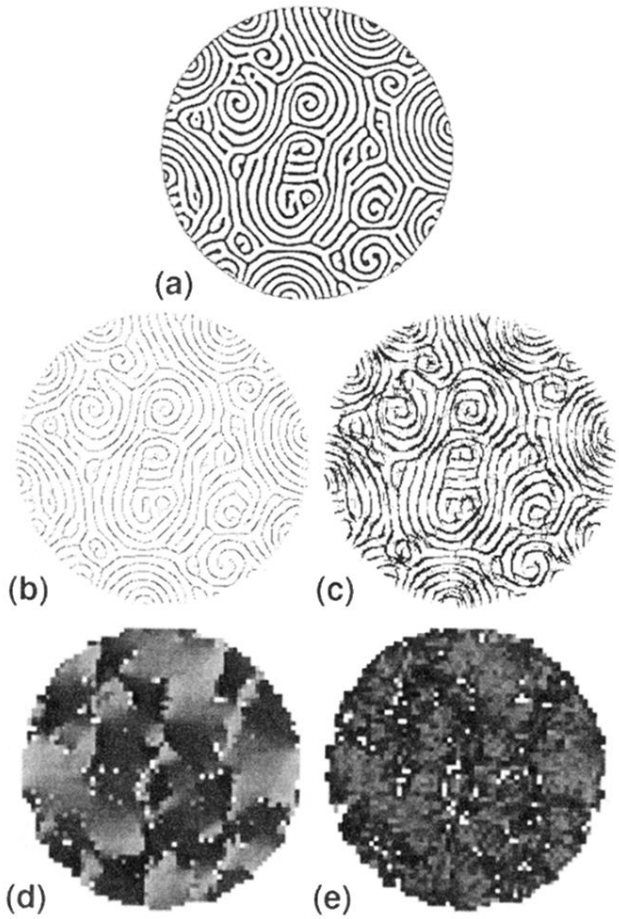

FIG. 16. Illustration of the procedure for determining roll orientation and curvature. The image is for $\epsilon=0.88$. (a) Original thresholded image, (b) skeleton-line image, (c) reconstruction of image based on calculated local roll orientations, (d) roll orientations (darker equals small angle with zero angle corresponding to the horizontal axis), and (e) curvatures (darker equals large curvature).

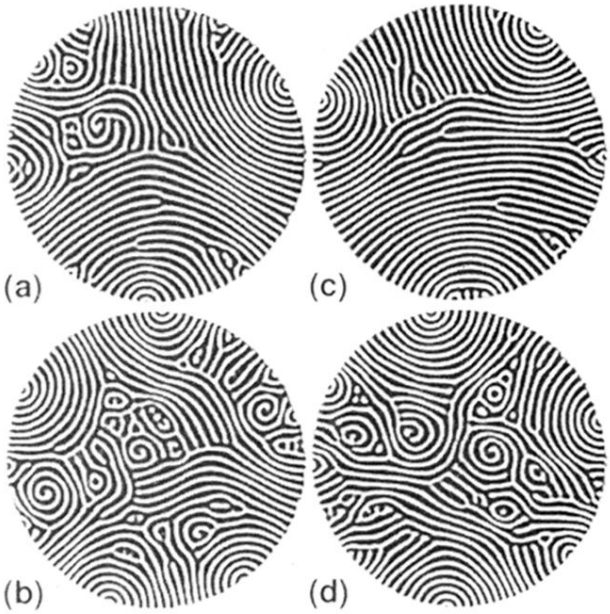

FIG. 18. Representative images at $\epsilon=0.73$. (a)–(d) correspond to the points indicated in Fig. 22.

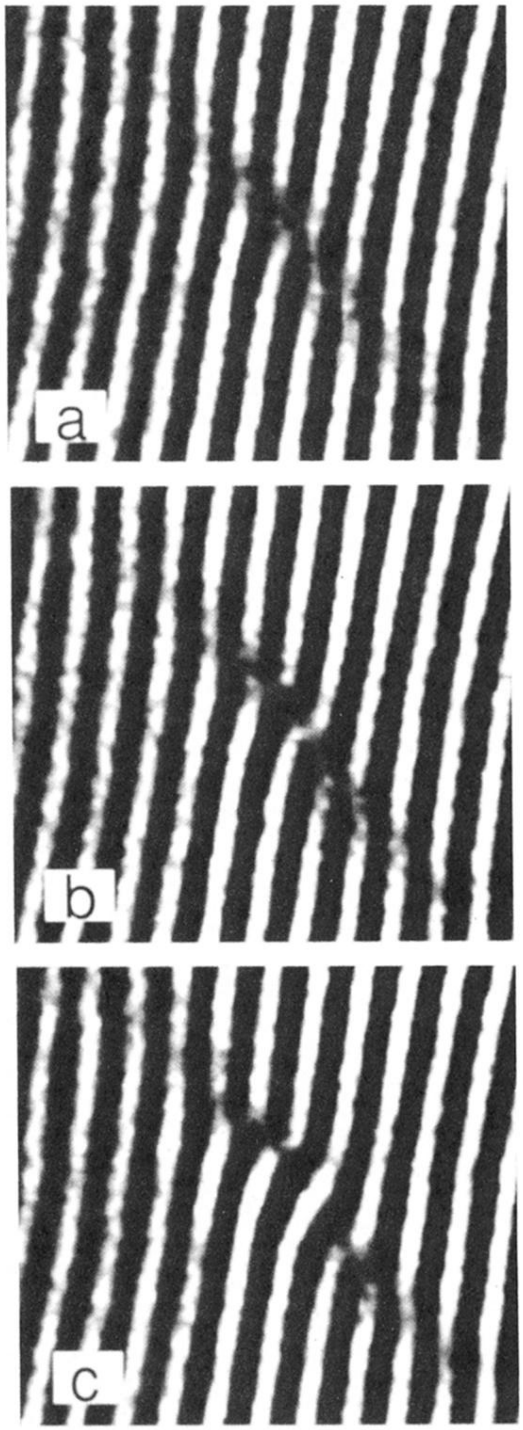

FIG. 2. Defect nucleation mechanism for straight rolls at $\epsilon=0.115$ and for $\Gamma=41$. A fraction of the total image, about $22d$ on a side, is shown. Elapsed times (arb. orig.) are (a) 0.0, (b) 1.3, and (c) $2.6\tau_v$.

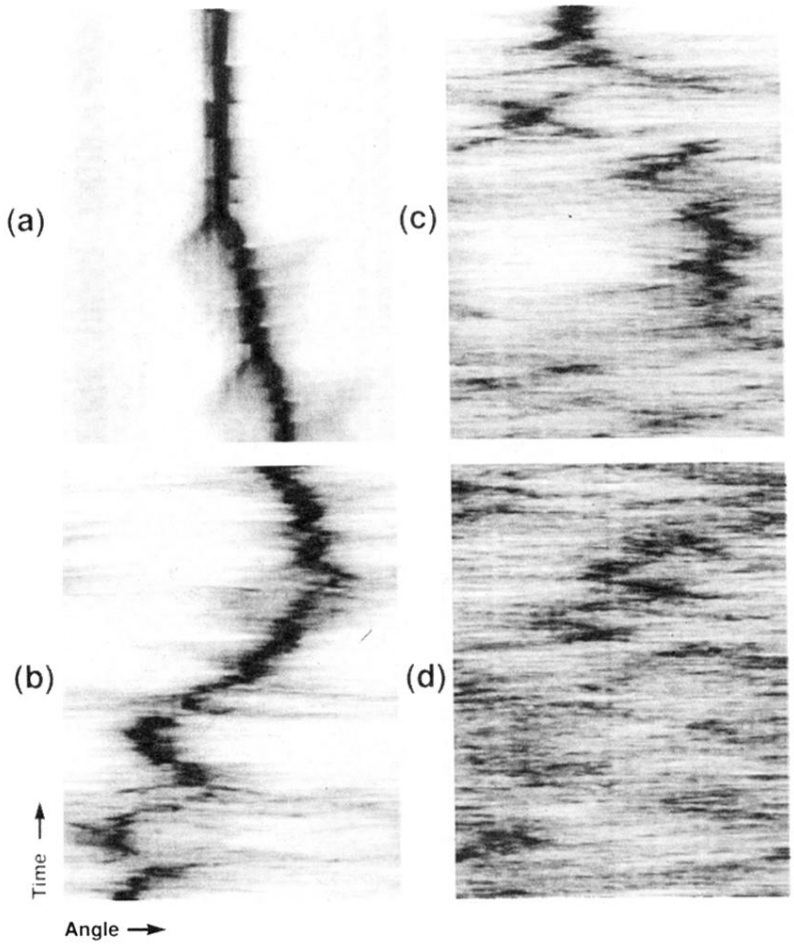

FIG. 3. Gray-scale plot (black:high) of the angular distribution ($0<\theta<\pi$) of the modulus of the Fourier transform as a function of time. The ϵ values and the total time covered are (a) $\epsilon=0.12$, $6.0\tau_h$; (b) $\epsilon=0.61$, $11.4\tau_h$; (c) $\epsilon=0.69$, $11.4\tau_h$; and (d) $\epsilon=0.78$, $11.4\tau_h$.

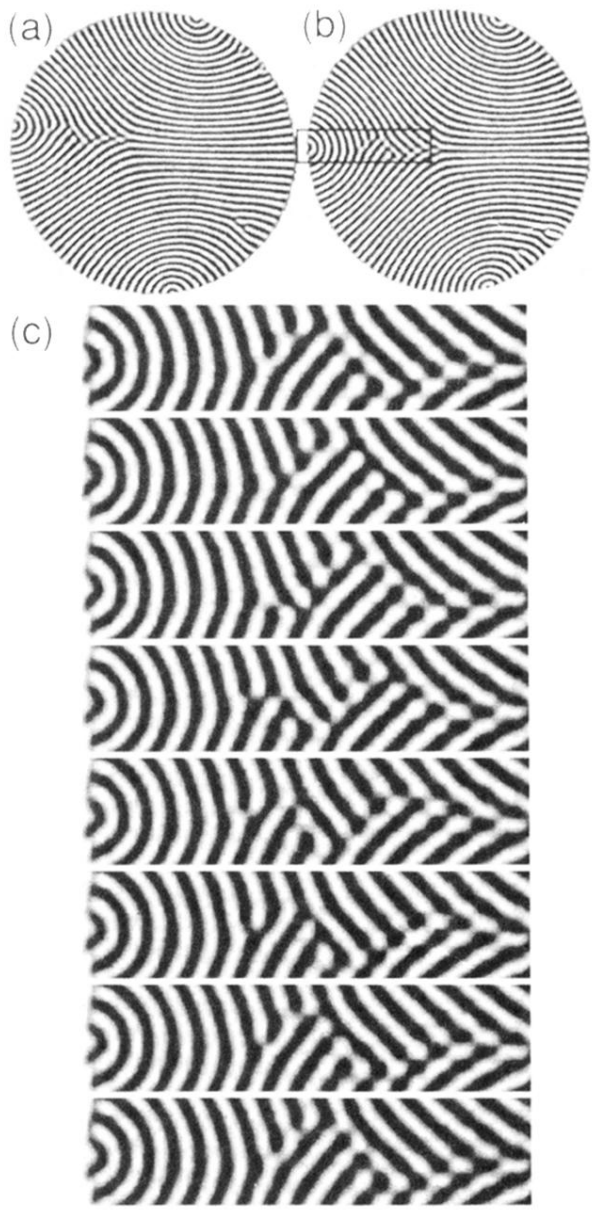

FIG. 5. Representative 3-foci patterns. (a) and (b) are separated in time by $6000\tau_v$. (c) A time sequence, $48\tau_v$ apart, of the region outlined in (b). The top image in (c) corresponds to the image enclosed by the box in (b).

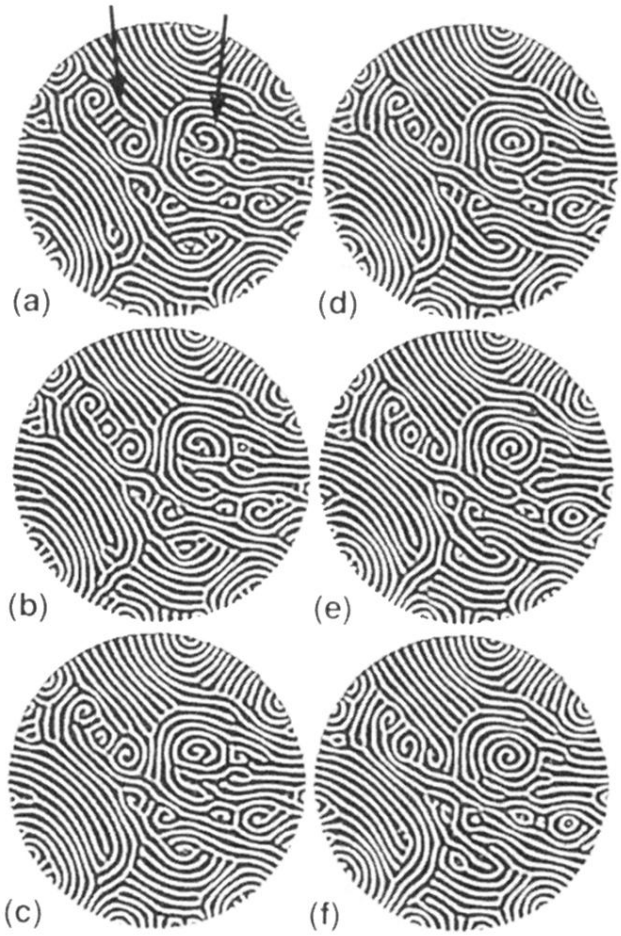

FIG. 6. Formation of spirals at $\epsilon=0.70$. The images are $6.4\tau_v$ apart. The arrows point to two structures that evolved into spirals.

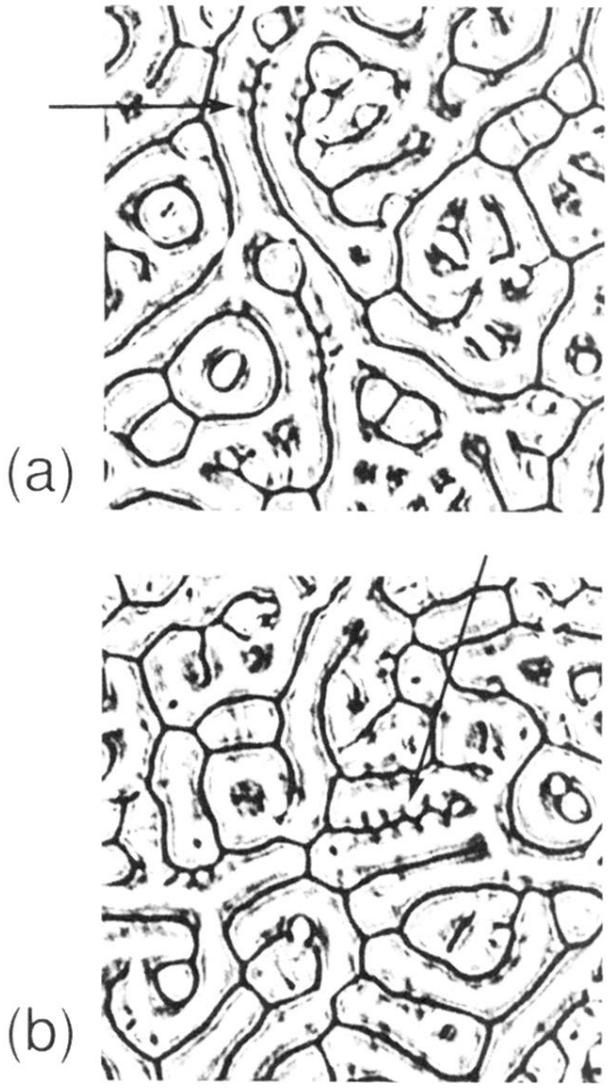

FIG. 7. Oscillatory instability at $\epsilon \approx 4.0$. The images are $78\tau_v$ apart. The arrows indicate the traveling waves.